
Master's Thesis in Theoretical Physics

# Hybrid Monte Carlo Simulations of Graphene

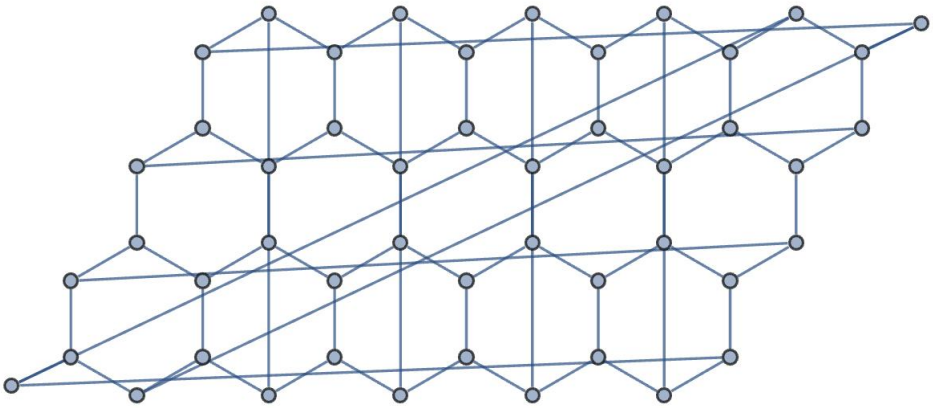

**Written by**
*R.S.Breebaart*

**under the supervision of**
Lars Fritz

January 27, 2023

**Abstract**

We give a discussion on the Hybrid Monte Carlo simulations of the tight binding model with Coulomb interactions, for the electronic properties of Graphene. The aim of our simulations is to determine the phase transition in which Graphene goes from a semimetal to an insulator through spontaneous breaking of sublattice symmetry. This is done non-perturbatively using lattice field theory techniques, working in the path-integral formalism with discrete euclidean time. We explain the method by [Brower, Rebbi and Schaich, arXiv:1101.5131v1, 26 Jan 2011] through which the theory of Graphene can be written in a form independent of a sign problem. An implementation of this method has been made in `Julia`, and can be found in [`https://github.com/Rik-Breebaart/GrapheneHMC.git`]. Our measurements show no clear phase-transition in the order parameters for this sublattice symmetry breaking. However, the system sizes on which the simulation have been performed where to small to make conclusive prediction on the presence and critical value of the phase-transition.

# Contents


**1 Introduction** **3**
- 1.1 What is Graphene? . . . 3
- 1.2 Tight-binding model of Graphene . . . 4
- 1.3 Phase transition . . . 7

**2 Monte Carlo Integration** **9**
- 2.1 Introduction . . . 9
- 2.2 Conventional numerical integration . . . 9
- 2.3 Monte Carlo integration . . . 9
- 2.4 Importance Sampling . . . 11
- 2.5 Sampling random variables . . . 12
  - 2.5.1 Inversion method . . . 12
  - 2.5.2 Rejection method . . . 13
  - 2.5.3 Markov Chain Monte Carlo . . . 13
  - 2.5.4 Hybrid Monte Carlo . . . 15

**3 Lattice Field Theory** **18**
- 3.1 Path-integral formalism . . . 18
- 3.2 Sign Problem . . . 21
- 3.3 Limits . . . 22

**4 Graphene** **24**
- 4.1 Graphene lattice . . . 24
- 4.2 Tight-binding Hamiltonian . . . 25
- 4.3 Lattice field theory of Graphene . . . 27
- 4.4 Coulomb potential . . . 29
- 4.5 Hybrid Monte Carlo for Graphene . . . 30
- 4.6 Observables . . . 32
  - 4.6.1 Expectations . . . 36

**5 Non-interacting Graphene** **38**
- 5.1 Non-interacting Tight-binding model of Graphene . . . 38
  - 5.1.1 Fermionic matrix Green's function . . . 39
  - 5.1.2 Fourier transforms . . . 39
- 5.2 Green's function . . . 40
- 5.3 Sublattice spin difference . . . 40

**6 Results** **43**
- 6.1 Antiferromagnetic spin $\langle S^3_- \rangle$ . . . 44
- 6.2 Thermodynamic limit . . . 45
- 6.3 Mass extrapolation . . . 46

**7 Conclusion** **47**

**8 Discussion** **48**

**Bibliography** **52**

**A Integration Saxton Weingarten** **55**

**B Hubbard-Stratonovich transformation** **56**

**C Sublattice spin difference results at different masses** **58**

# Chapter 1

# Introduction

## 1.1 What is Graphene?

For a long time, two-dimensional materials consisting of a single layer of atoms were considered to be impossible. Nevertheless, in 2004, Novoselov and Geim[1] realized such a material. The 2D material which they realized was named Graphene, as it was created by isolating a single layer from the 3D material Graphite. Graphene consists of a single layer of carbon atoms arranged on a hexagonal (Honeycomb) lattice. The study of Graphene became, since 2004, an active field of research in the field of condensed matter, both theoretically and experimentally. Graphene has been considered as one of the most promising materials of the twenty-first century. It being the first truly 2D material, a large amount of research has been done in determining the key properties of the material. Graphene has since then gained its popularity due to the mechanical and transport properties it possesses. It is flexible and light weight, yet strong among other key characteristics[2]. The flexibility which Graphene possesses is reflected in it electronic properties. A $\sigma$ bond of the $sp^2$ hybridization is generated between the carbon atoms, leading to the trigonal planar structure with a distance of $a = 1.41$Åbetween each carbon atom. The $\sigma$ band is responsible for the flexibility and robustness of the lattice structure between the atoms. The $p$ orbital perpendicular to the trigonal plane, can bind covalently with neighboring carbon atoms, participating in a $\pi$ band, which is half-filled.

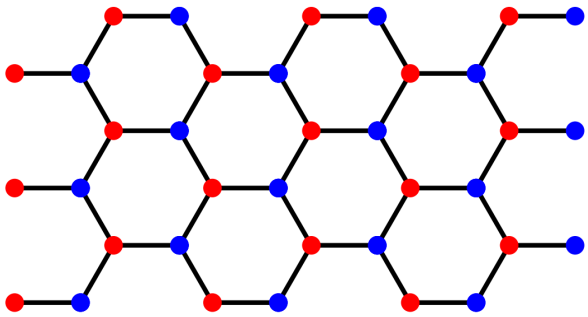

Figure 1.1: The hexagonal lattice structure of Graphene[3]

The large number of electronic and mechanical properties of Graphene make it a great candidate for a wide range of technological applications (for an extensive review on Graphene and its properties, see Ref.[2, 4])

Graphene at half-filling has a strong tight-binding character with large Coulomb energies, leading to strong collective effects such as magnetism and insulating behavior due to correlation gaps or Mottness[2]. When considering Graphene in a non-interacting frame, the electrons behave as Dirac quasiparticles, with a linear dispersion around Dirac points. At half-filling, the chemical potential exactly crosses these Dirac points. This dispersion, only possible at low energy, mimics the physics of

quantum electrodydynamics (QED) for massless fermions, however these fermions move with a speed $v_f \approx c/300$, where $c$ is the speed of light.

Graphene at half-filling can be efficiently simulated using Hybrid Monte Carlo (HMC), an algorithm widely used in the field of lattice gauge theory[5, 6, 7, 8]. This simulation technique allows us to look at Graphene in a non-perturbative manner, being able to investigate the effect of interactions at strong coupling.

A relevant question which has immediate consequences in technological developments is whether Graphene, which is known to be an electronic conductor when attached to a substrate, can develop a band gap under the right circumstances. Attaching Graphene to a certain substrate will induce a dielectric screening which lowers the *effective* fine-structure constant $\alpha_{\text{eff}}$ of the system. The expectation is that when this screening is reduced and $\alpha_{\text{eff}}$ becomes larger than some critical $\alpha_c$, a phase transition to a gapped phase occurs.

Experiments on Graphene in vacuum in which the fine-structure constant is $\alpha_{eff,0} \approx 300/137 \approx 2.2$ have proven that it is a conductor[9]. However, analytical calculations and simulations, which assumed that the electromagnetic interactions of $\pi$-band electrons are essentially unmodified Coulomb interactions, support the scenario of a gapped phase at $\alpha_{eff,0} > \alpha_c \approx 1$. Since this gapped phase is not observed in experiments, this difference must be investigated. It was suggested by Ref.[10] to include $\sigma$-band screening, which moves $\alpha_c$ to larger values. To do so, they modified the Coulomb-interaction to account for the $\sigma$-band screening. In Ref.[11], a modified partially screened Coulomb potential was used which uses results from calculations within the constrained random phase approximation (cRPA)[12] for the short distance interactions.

In this work, we will conduct simulations similar to those in Ref.[5], using their modified partially screened Coulomb-interaction. They used a phenomenological model given in Ref.[12] to construct a partially screened Coulomb potential, which uses a momentum based dielectric constant that smoothly turns into the unscreened Coulomb potential at the long-wavelength limit. Our aim is to give a comprehensive description of the lattice field theory (LFT) approach used for the study of Graphene at strong coupling. Our work is structured as follows; we will first look at non-interacting Graphene, its dispersion and Dirac cones and how introducing a mass induces a gap ("mass gap") in the dispersion. This will be followed by a description of the numerical integration tools needed to perform the lattice field theory calculations of Graphene. Here a description of the HMC algorithm is given in general context. Next, we will describe the general concept of a lattice field theory of fermions at low-energy finite temperature. An important issue which arises in these methods will be discussed, the "sign-problem". This "sign-problem" greatly hinders the advances that can be made in the use of lattice field theory calculations, allowing it to be used only in specific cases. Once we have gathered the theoretical knowledge needed for an LFT of Graphene, we will introduce the specifics and modifications needed to perform the HMC calculations, with the aim to remove the "sign-problem". When the theory is written in a manner suitable for HMC calculations, we will proceed in a description on how these calculations are performed and what relevant order-parameters we need to investigate in the aim of finding a phase transition. Finally, we will investigate our numerical results in which no clear phase transition was found. A discussion will be given on the specifics of the simulations, their shortcomings and what can be learned from them.

## 1.2 Tight-binding model of Graphene

Theoretically Graphene can be described by the tight-binding (TB) model, which describes the hopping of free electrons from one lattice site to another neighboring site. For the spinless case, the tight-binding Hamiltonian in second quantization is written as

$$H_{tb} = -\kappa \sum_{\langle x,y \rangle} (a_x^\dagger a_y + a_y^\dagger a_x), \tag{1.1}$$

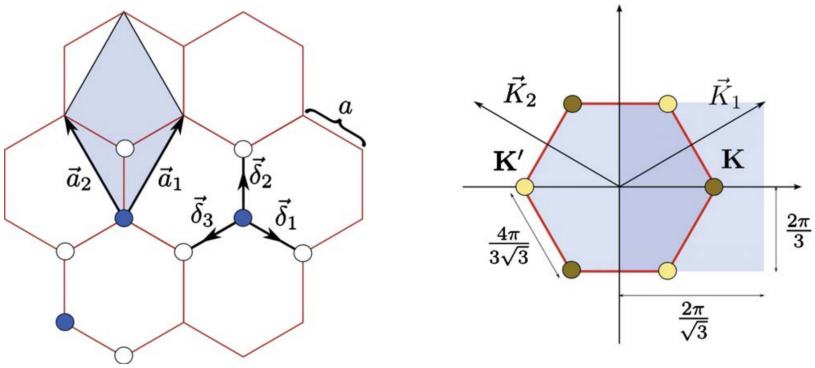


Figure 1.2: The Hexagonal Real-space lattice and Brillouin zone of Graphene. Left: The Hexagonal lattice with nearest neighbors $\delta_i$, primitive vectors $a_i$ and lattice spacing $a \approx 1.41$Å. Right: The Brillouin zone of Graphene, with Dirac points $\mathbf{K}$ and $\mathbf{K}'$. Figure taken from Ref.[4]

where the summation $\langle x, y\rangle$ is over nearest neighbors and the parameters $\kappa$ is the hopping amplitude. For Graphene this amplitude is $\kappa \approx 2.8$eV[2].

The Hexagonal structure of Graphene can be described in terms of a triangular lattice with a basis of two atoms per unit cell, which we label as A and B, creating two triangular sublattice of the atoms. The lattice vectors can be written as

$$a_1 = \tfrac{a}{2}(3, \sqrt{3}), \quad a_2 = \tfrac{a}{2}(3, -\sqrt{3}). \tag{1.2}$$

The hopping between the electrons occurs between their neighboring sites, for which the three nearest-neighbor vectors for an atoms on lattice $A$ are given by

$$\delta_1 = \tfrac{a}{2}(1, \sqrt{3}), \quad \delta_2 = \tfrac{a}{2}(1, -\sqrt{3}) \text{ and } \quad \delta_3 = -a(1, 0). \tag{1.3}$$

We can write the TB Hamiltonian in terms of these neighbor vectors,

$$\begin{aligned} H_{tb} =& -\kappa \sum_{x\in A}\sum_{\delta_A}(a_x^\dagger a_{x+\delta_A} + a_{x+\delta_A}^\dagger a_x) \\ =& -\kappa \left(\sum_{x\in A}\sum_{\delta_A} a_x^\dagger a_{x+\delta_A} + \sum_{x\in B}\sum_{\delta_B} a_x^\dagger a_{x+\delta_B}\right), \end{aligned} \tag{1.4}$$

where the sum over $\delta_A(\delta_B)$ is carried over the nearest-neighbor vectors surrounding the A (B) lattice points. The nearest-neighbor vectors are related by $\delta_B = -\delta_A$.

Presenting the creation operator as $\psi_x^\dagger = (a_x^{A,\dagger}, a_{x+\delta_3}^{B,\dagger})^T$, where $x$ lives on the A sublattice (the unit cell) and $x + \delta_3$ is the site on the B sublattice.

Now going to k-space, using that

$$a_x^\dagger = \frac{1}{\sqrt{N}} \sum_{k\in BZ} e^{ikx} a_k^\dagger, \tag{1.5}$$

where $N$ is the number of unit cells and the sum runs over the Brillouin zone, which is shown in Fig.1.2. The resulting Hamiltonian of the TB model in k-space is

$$\begin{aligned} H_{tb} =& -\kappa \frac{1}{N} \sum_{x\in A}\sum_{\delta_A}\Big(\sum_{k\in BZ} e^{ik\ x} a_k^{A,\dagger} \sum_{k'\in BZ} e^{-ik'\ (x+\delta_A)} a_{k'}^B + \sum_{k\in BZ} e^{ik\ (x+\delta_A)} a_k^{B,\dagger} \sum_{k'\in BZ} e^{-ik'\ x} a_{A,k'}\Big) \\ =& -\kappa \frac{1}{N} \sum_{k,k'\in BZ}\sum_{x\in A}\sum_{\delta_A}(e^{i(k-k')x - ik'\delta_A} a_k^{A,\dagger} a_{k'}^B + e^{i(k'-k)x + ik'\delta_A} a_k^{B,\dagger} a_{k'}^A) \\ =& -\kappa \sum_{k\in BZ}\sum_{\delta_A}(e^{-ik\ \delta_A} a_k^{A,\dagger} a_k^B + e^{ik\ \delta_A} a_k^{B,\dagger} a_k^A), \end{aligned} \tag{1.6}$$

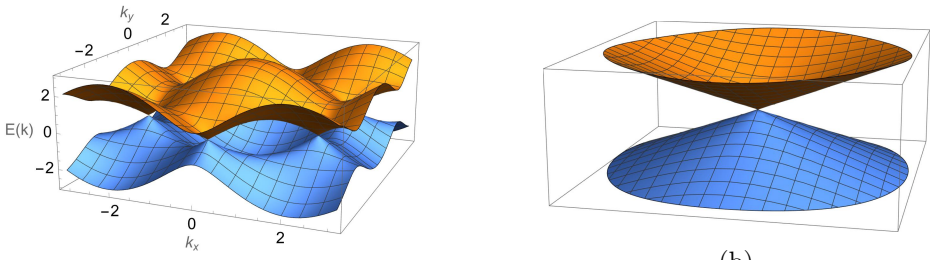


(a) (b)

Figure 1.3: (a) Electronic dispersion on the honeycomb lattice. (b) Linear dispersion around the Dirac Points where $E_\pm \approx \pm v_f|\mathbf{q}|$.

where we used that

$$\frac{1}{N}\sum_{x\in A} e^{i(k-k')x} = \delta_{k,k'}.$$

We can therefore write the TB Hamiltonian in k-space in matrix notation as

$$H_{tb} = \sum_{k\in BZ} \psi_k^\dagger h_k^{(tb)} \psi_k, \tag{1.7}$$

where $\psi_k^\dagger = (a^{A,\dagger}, a^{B,\dagger})^T$ and

$$h_k^{(tb)} = -\kappa \begin{pmatrix} 0 & \Delta_k \\ \Delta_k^* & 0 \end{pmatrix} \quad \text{with} \quad \Delta_k = \textstyle\sum_{\delta_A} e^{-ik\ \delta_A} \tag{1.8}$$

The two electronic bands of this matrix can be obtained by computing the eigenvalues of Eq.(1.8), resulting in

$$E_\pm(k) = \pm\kappa\sqrt{3 + f(k)} \tag{1.9}$$

with

$$f(k) = 2\cos\left(\sqrt{3}k_y a\right) + 4\cos\left(\frac{3}{2}k_x a\right)\cos\left(\frac{\sqrt{3}}{2}k_y a\right). \tag{1.10}$$

The two electron bands are symmetric around $E = 0$, touching each other at two single points in the Brillouin zone, the Dirac points

$$\mathbf{K} = (\tfrac{2\pi}{3a}, \tfrac{2\pi}{3\sqrt{3}a}), \quad \mathbf{K}' = (\tfrac{2\pi}{3a}, -\tfrac{2\pi}{3\sqrt{3}a}). \tag{1.11}$$

In Fig.1.3, we show the full band structure and a zoom in close to one of the Dirac points. The dispersion around the Dirac Points can be obtained by expanding the band structure Eq.(1.9) close to the $\mathbf{K}$ (or $\mathbf{K}'$) points, as $\mathbf{k} = \mathbf{K} + \mathbf{q}$, with $|\mathbf{q}| \ll \mathbf{K}$[13],

$$E_\pm \approx \pm v_f|\mathbf{q}| \tag{1.12}$$

where $\mathbf{q}$ is the momentum relative to the Dirac points and $v_f$ the Fermi-velocity. In the region around the Dirac points, electrons behave as massless particles propagating with a velocity given by $v_f = 3\kappa a/2$, with a value of $v_f \approx c/300$ m/s, where $c$ is the speed of light.

We can introduce a gap into the dispersion around the Dirac points by adding a mass which is staggered between the two sublattices,

$$H_m = \sum_x m_x (a_x^\dagger a_x) \tag{1.13}$$

with

$$m_x = \begin{cases} +m, & x \in A \\ -m, & x \in B. \end{cases} \tag{1.14}$$

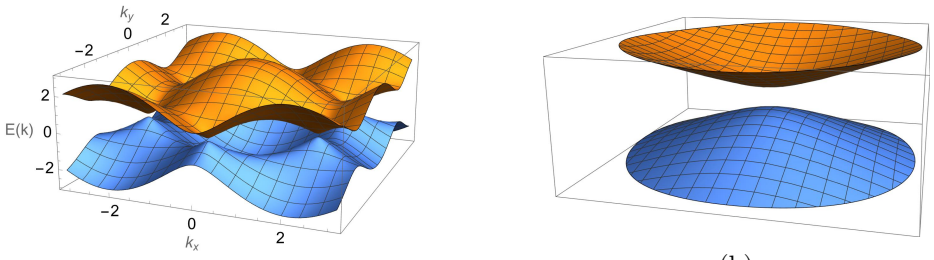


(a) (b)

Figure 1.4: (a) Electronic dispersion on the honeycomb lattice with an added mass gap. (b) Gapped dispersion around the Dirac Point.

Going to k-space this Hamiltonian becomes

$$H_m = \sum_{k \in BZ} \psi_k^\dagger h_k^{(m)} \psi_k, \tag{1.15}$$

with

$$h_k^{(m)} = \begin{pmatrix} m & 0 \\ 0 & -m \end{pmatrix}. \tag{1.16}$$

Adding this to the TB model leads to the following Hamiltonian in momentum space,

$$H = \sum_{k \in BZ} \psi_k^\dagger (h_k^{(tb)} + h_k^{(m)}) \psi_k. \tag{1.17}$$

The electronic band structure with this added staggered mass is given by

$$E_\pm(k) = \pm\sqrt{3 + m^2 + f(k)}, \tag{1.18}$$

where $f(k)$ is Eq.(1.10). In Fig.1.4, we show the full band structure when a mass gap is introduced and the dispersion around the Dirac points.

## 1.3 Phase transition

We now have an understanding of how Graphene acts in the non-interacting case. The dispersion around the Dirac points behaves linearly with a fermi velocity $v_f \approx c/300$. The non-interacting theory of Graphene can therefore be related to the Quantum Electro Dynamics (QED) theory of free fermions. The fine-structure constant quantifies the strength of electromagnetic interactions between charged particles. In QED, the fine-structure constant is

$$\alpha = \frac{e^2}{4\pi\epsilon_0 \hbar c} \approx \frac{1}{137}, \tag{1.19}$$

where $e$ is the elementary charge, $\hbar$ the reduced planks constant, $c$ the speed of light and $\epsilon_0$ the dielectric constant in vacuum. The fine-structure constant $\alpha$ in QED is small enough such that, either the electromagnetic interactions can be neglected or perturbative methods can be used.

Since the electrons in Graphene behave as free fermions, we can also determine an *effective* fine-structure constant for Graphene, in which we now have fermions with velocity $v_f$ instead of the speed of light $c$. In vacuum the *effective* fine-structure constant for Graphene is

$$\alpha_{\text{eff}} = \frac{e^2}{4\pi\epsilon_0 \hbar v_f} \approx \frac{300}{137} \approx 2.2, \tag{1.20}$$

since $v_f \approx c/300$. The fine-structure constant $\alpha_{\text{eff}}$ in Graphene is considerably larger than that in QED, and we can not simply ignore the electromagnetic interactions. Graphene in its non-interacting case, obeys sublattice symmetry, meaning that the system remains identical when exchanging particles

between the A and B lattices. This symmetry is broken at strong coupling, and a mass-gap would appear. This symmetry breaking transitions the system from a conductor to an insulator. To look at the influence of the interactions on the system, path-integral formalism is often used. In analytical calculations, the interactions are treated through the use of a mean field approximation or other perturbative methods. However, in this work we will be looking at the influence of the interaction by means of a lattice field theory approach. The goal is to determine the expectation value of the relevant observable which quantifies sublattice symmetry breaking. The observables in a field theory are computed as

$$\langle O \rangle = \int \mathcal{D}\phi O(\phi) e^{-S[\phi]} \tag{1.21}$$

where $\mathcal{D}\phi$ denotes the integration measure over all possible world-lines or paths of the field variable $\phi$, $O(\phi)$ is a functional form of the observable and $S(\phi)$ the action which describes the world-line or path that is most likely to occur. In the lattice field theory approach, the paths are discrete working with a finite number of lattice points and temporal time slices. The field variables are stored on a computer and numerical integration techniques are used to compute the expectation value of the observable. In the following chapter, we will discuss numerical integration, which is needed to compute the expectation values.

A few comments on the units and conventions used throughout this report: We use the Gaussian system of electromagnetic units in which the Coulomb potential is $1/r$, which implies the relation $\alpha = e^2 \approx 1/137$ between the elementary charge and the (dimensionless) fine structure constant. All physical quantities can therefore be expressed in terms of a basic unit of energy or length. Throughout this work, we will express our quantities in terms of electron-volt (eV), using the relation $10^{-7}\text{m} \approx 0.506\text{eV}^{-1}$. We use the natural system of units as used in high-energy physics, i.e. $c \equiv 1$ and $\hbar \equiv 1$.

# Chapter 2

# Monte Carlo Integration

## 2.1 Introduction

This chapter will discuss a numerical strategy to compute large dimensional integrals. The method we will be discussing is that of *Monte Carlo*(MC) integration , which uses statistical averages by taking random samples and statistical statements to obtain an estimate numerical value for the integral.

All the strategies of numerical integration approximate integrals by dealing with the integral as a weighted sum of functional values:

$$\int_{\Omega} f(\mathbf{x})d\mathbf{x} \approx \sum_{i \in E} w_i f(\mathbf{x_i}), \tag{2.1}$$

where $\Omega \in \mathbb{R}^D$ is the integration domain, $f$ the integrand, $E$ a finite set up indices, $x_i$ points in $\Omega$ and $w_i$ weights associated to these points. Conventional numerical integration or quadrature integration uses points on an equidistant grid, while Monte Carlo integration selects random points.

## 2.2 Conventional numerical integration

To better understand why Monte Carlo integration is used, a brief understanding of conventional numerical integrations is useful. In conventional numerical integration, the integral is approximated by taking uniformly distributed points $x_i$ on an equidistantly spaced grid inside the integral domain $\Omega$. The points are weighted by interpolating between the different points often using a polynomial interpolation function of low degree. An example of methods of interpolation that are used are the midpoint rule or the trapezoidal rule, where this interpolation is applied repeatedly between the different points. When integrating on a $D$ dimensional domain by taking $N$ sampling points per dimension the trapezoidal rule has an error of $\mathcal{O}(N^{-2/D})$[14].

## 2.3 Monte Carlo integration

In the case of a high dimensional integral, the number of points needed to compute the integral with relative accuracy becomes quickly intractable. To overcome this problem, *Monte Carlo Integration* is introduced.

Monte Carlo integration is a stochastic integration method relying on randomness to perform the integrations. Instead of using evenly distributed points in the $D$ dimensional space, the integral is approximated by taking $x_i$ from a certain probability distribution $p(x)$ with a weight $w_i$ related to this distribution. A simple example of this would be to approximate "pi" by uniformly throwing "darts" ($x_i$ points) at a square board and counting the points which are located inside the unit circle (see fig.2.2).

Aiming to compute the area of the unit circle ($A = \pi$) through an integral as

$$A = \int_{-1}^{1} \int_{-1}^{1} f(\mathbf{x})d\mathbf{x}, \tag{2.2}$$

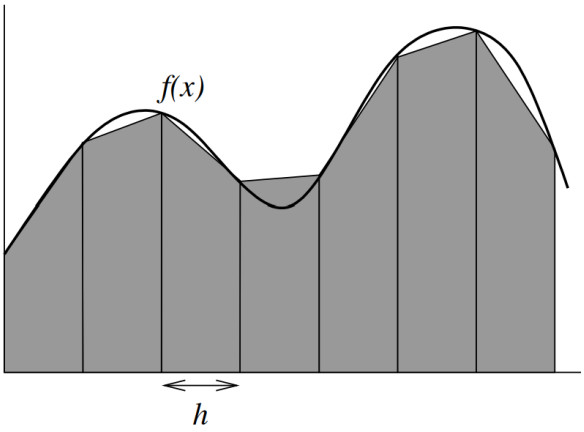


Figure 2.1: Example figure of conventional numerical integration taken from Ref.[14]

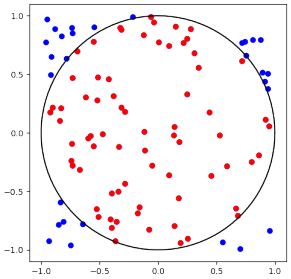

Figure 2.2: Simple example of Monte Carlo integration to approximate "pi" by counting the points inside the unit circle.

with the integrand one for the surface of the unit circle and zero outside

$$f(\mathbf{x}) = \begin{cases} 1, & \text{if } \mathbf{x}^2 \leq 1 \\ 0, & \text{otherwise} \end{cases}. \tag{2.3}$$

Solving this integral using uniformly distributed samples between $[-1, 1]$ with a density function

$$u(\mathbf{x}) = \begin{cases} \frac{1}{4}, & \text{if } \mathbf{x} \in [-1, 1]^2 \\ 0, & \text{otherwise,} \end{cases} \tag{2.4}$$

would lead to an approximation of the integral as

$$A \approx \frac{1}{N} \sum_{i=1}^{N} \frac{1}{u(\mathbf{x}_i)} f(\mathbf{x}_i) = 4 \frac{N_{hit}}{N}, \tag{2.5}$$

which is the ratio between the "darts" which fall inside the unit circle ($N_{hit}$) and the total number of "darts" thrown ($N$) multiplied by the area in which the "darts" are thrown. In the table below an example of performing this approximation to "pi" is shown for different number of sample points $N$.

The Monte Carlo method clearly gives approximate results, where the accuracy strongly depends on the number of points $N$. The Monte Carlo method can be described by computing an expectation value (or average) as

$$\langle f \rangle = \frac{1}{N} \sum_{i=1}^{N} f(x_i). \tag{2.6}$$

| N | $A$ | Error |
|---|---|---|
| 10 | 3.040000 | 0.012400 |
| 100 | 3.146000 | 0.001083 |
| 1000 | 3.126800 | 0.000148 |
| 10000 | 3.141620 | 0.000009 |
| 100000 | 3.142664 | 0.000001 |

A good measure for the error of this expectation value is based on the sample variance $\sigma_f^2$ with $\sigma_f$ the standard deviation from the mean, given by the unbiased estimate of the variance

$$\mathrm{Var}(f) \equiv \sigma_f^2 = \frac{1}{N-1}\sum_{i=1}^{N}(f(x_i) - \langle f\rangle)^2 = \langle f^2\rangle - \langle f\rangle^2, \tag{2.7}$$

with

$$\langle f^2\rangle = \frac{1}{N}\sum_{i=1}^{N} f(x_i)^2. \tag{2.8}$$

A good measure for the error of our integral $I$, would be the variance of $M$ measurements of the integral, each with $N$ points sampled. According to the central limit theorem, these integral values would be normally distributed around the mean $\langle I\rangle$. Again a good measure of the difference to the mean would be the standard deviation. Using that variance is additive if the different terms are uncorrelated then we can obtain that the variance of the integral $I$ is given by

$$\mathrm{Var}(I) = \frac{\mathrm{Var}(f)}{N}, \tag{2.9}$$

such that a good measure for the error of our integral approximation is

$$\delta I = \sqrt{\mathrm{Var}(I)} = \sqrt{\frac{\langle f^2\rangle - \langle f\rangle^2}{N}}. \tag{2.10}$$

It is important to note that the error on the approximation is not a strict error bound, the integral approximation using random sampling may not uncover all the important features of the integrand, leading to an underestimated error.

Computing an integral using these random points thus leads to an error of $\mathcal{O}(N^{-1/2})$, with $N$ the total number of samples. This error is independent of the dimensionality of the problem, leading to an improved error compared to the trapezoidal rule when $D > 8$.

The example of approximating "pi" uses a uniform distribution from which the samples are taken. However, this is not always necessary. In cases where the function contains a large amount of peaks and valleys it might be more useful to sample from a distribution reflecting these shapes. Ensuring that the weights associated to the samples is scaled for the peaks and valleys requiring less points. This method of using a weight associated to the distribution is known as *importance sampling*, sampling the points relevant to the integral with a higher probability.

## 2.4 Importance Sampling

In the previous section we showed that you could approximate "pi" by taking a weighted ratio of the number of hits in the unit circle and total number of throws on a square board. The weight used to determine the value of the integral was determined by the distribution used for the sampling. Similarly, we can for simplicity consider a 1-dimensional integral

$$\int_a^b f(x)dx, \tag{2.11}$$

which we can rewrite as

$$\int_a^b f(x)dx = \int_a^b g(x)q(x)dx \quad \text{with} \quad g(x) \equiv \tfrac{f(x)}{q(x)} \quad (x \in [a,b]). \tag{2.12}$$

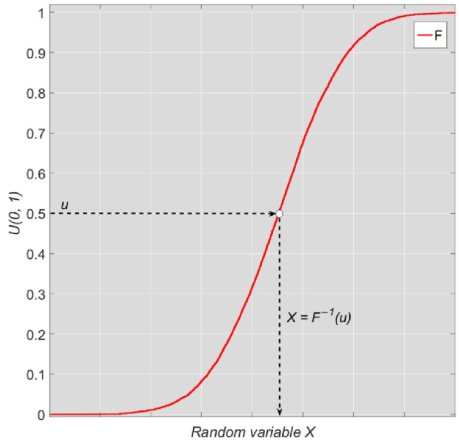


Figure 2.3: Illustration of the inversion method taken from Ref.[16]

To approximate the integral, we could now sample points $Q_i$ from a distribution $q(Q)$ between $[a, b]$, such that we can compute the integral as

$$\int_a^b f(x)dx \approx \frac{1}{N}\sum_{i=1}^{N} g(Q_i). \tag{2.13}$$

Computing the integral in this manner is the same as taking an expectation value of the function $g(x)$ with distribution $q$. Sampling points according to $q$ and computing the average of $g(x)$ with respect to these points.
We can see that since the points $Q_i$ are sampled from $q$, the points with higher probability in $q$ are sampled more often but with a lower weight and those with small probability are only sampled sometimes but with higher contribution. By taking these weights related to the distribution the result will go to the average by virtue of the central limit theorem.

## 2.5 Sampling random variables

There are a variety of techniques in sampling random numbers. The most important problem these methods overcome is that computers can not simply generate non-uniform random numbers.

Uniformly distributed random numbers are computed using *pseudo* random number generators. These random numbers are then not actually random, but follow some specific mathematical method, creating each successive number from the previous number. Examples of such methods are Linear Congruential Generators or xorshift[15]. These methods generate a sequence of numbers which, satisfy the randomness test, allowing them to be used as uniformly distributed random numbers.

The main problem however arrives when dealing with non-uniformly distributed numbers. To sample numbers from a non-uniform distribution, the uniformly distributed numbers generated should be used to do so.

### 2.5.1 Inversion method

One of the methods to sample from a non-uniform distribution is the inversion method, in which the cumulative distribution function (cdf),

$$F_f(x) = \int_{-\infty}^{x} f(y)dy \tag{2.14}$$

is related to a uniformly distributed number $u \in [0, 1]$. For the cdf we know that the integral over the full space will always be 1, and we thus have that for some $x_i$ distributed according to $f$ that

$$F_f(x_i) = u_i. \tag{2.15}$$

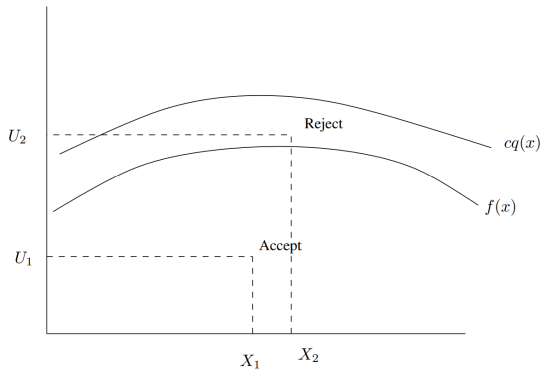


Figure 2.4: Illustration of the rejection method taken from Ref.[14]

If we inverted the cdf then we can obtain a sample $x_i$ of the distribution $f$, by sampling a uniformly distributed number $u_i$, so

$$F_f(u_i)^{-1} = x_i. \tag{2.16}$$

An illustration of the inversion method is shown in Fig.2.3. This method, however, requires the distribution $f$ to be continuous and that the cdf is invertible analytically which is only true in some simple cases. An example distribution for which this method can be used is a Cauchy distribution.

### 2.5.2 Rejection method

This inversion method is thus only possible in some cases, another method used to sample a distribution is the *rejection* method[17]. The rejection method works by sampling from some convenient distribution $q$, scaled by some constant $c$, such that these points fall above the desired distribution $f$. The sample $X_i$ taken from distribution $q$ is accepted based on the ratio

$$\frac{f(Q_i)}{cq(Q_i)} \leq u_i$$

by taking a uniformly distributed random number $u_i \in [0, 1]$. An illustration of the rejection method is shown in Fig.2.4. One can easily see that this method would sample from the distribution $f$. However, it requires that the distribution $q$ is easy to sample and that $cq$ is close to the upper bound of $f$, as otherwise most samples are rejected. This thus also requires a good understanding of the desired distribution and its peaks.

### 2.5.3 Markov Chain Monte Carlo

This brings us to the third method of sampling from a distribution and the most relevant for this report: the *Metropolis* method (also known as *Markov chain monte carlo*). It is useful in sampling arbitrary distributions in a high dimensional space with the advantage that the density function does not need to be normalized. The main disadvantage of this method, is that the samples are created in a sequence where the previous sample is used to create the next sample (and thus a markov chain). The samples are, therefore, not fully independent and may be correlated.

To create samples from an arbitrary distribution the Markov Chain Monte Carlo (MCMC) method is often used. This method relies on creating samples in a sequence based on the previous sample and has the advantage that the distribution does not need to be normalized. The method by which the sequence of samples is created uses the Metropolis-Hastings algorithm[18].

If we aim to create a sequence of samples which satisfy a desired distribution $p(x)$, we can create a Markov chain of points where each point has a certain transition probability $P(x|x')$ to go from the previous configuration $x$ to the next $x'$. To ensure that this sequence of points asymptotically leads the desired distribution two conditions are required:

- The new sampled points should be from the stationary distribution $\pi(x)$, which asymptotically leads to the desired distribution $\pi(x) \to p(x)$.
- Any other configuration should be reachable in a finite number of steps and thus the whole configuration space can be searched (meaning the transitions should be ergodic).

These two conditions are satisfied when using the condition known as *detailed balance* which requires that the transition $x \to x'$ is reversible, such that the probability of transition from state $x$ to $x'$ is the same as going from $x'$ to $x$:

$$P(x'|x)p(x) = P(x|x')p(x'), \tag{2.17}$$

which can be rewritten as

$$\frac{P(x|x')}{P(x'|x)} = \frac{p(x)}{p(x')}, \tag{2.18}$$

which implies that the flux of samples $x$ transitioning to $x'$ is equal to that of $x'$ to $x$.

When performing a transition, this is usually done by updating the previous configuration by a small amount. We can express the transition probability in terms of a proposal distribution $T(x|x')$ and acceptance probability $A(x, x')$ as

$$P(x|x') = T(x|x')A(x', x). \tag{2.19}$$

The proposal probability is determined by the method in which the new sample is created, and the acceptance probability is given by the Metropolis-Hastings acceptance ratio.

This acceptance ratio can be found by rewriting the detailed balance condition using the rewritten transition probability Eq.(2.19), getting

$$\frac{A(x', x)}{A(x, x')} = \frac{T(x'|x)p(x)}{T(x|x')p(x')}. \tag{2.20}$$

An acceptance which satisfies this detailed balance condition is the Metropolis ratio[19]

$$A(x, x') = \min\left\{1, \frac{T(x'|x)p(x)}{T(x|x')p(x')}\right\}. \tag{2.21}$$

We can see that this acceptance satisfies the detailed balance, since either $A(x, x') = 1$ or $A(x', x) = 1$ and thus Eq.(2.20) always holds. Now in the case we choose a symmetric proposal distribution, where $T(x'|x) = T(x'|x)$, this results in the well known Metropolis-Hastings algorithm[18] with the acceptance rate

$$A(x, x') = \min\left\{1, \frac{p(x)}{p(x')}\right\}. \tag{2.22}$$

With this acceptance ratio, we can also see that the distribution does not need to be normalized as the normalization constants cancel. Now how do we apply this to obtain samples from our desired distribution $p(x)$? We could sample from any probability distribution by starting from a random initial configuration $x_0$ and performing an update $x_0 \to x_1$ according to our proposal distribution $T(x_0|x_1)$. This is often some small change $q$ taken from a symmetric distribution such as a Gaussian. Next, based on the acceptance ratio the sample is accepted if some uniformly distributed random number $u \in [0, 1]$ satisfies

$$A(x_0, x_1) \leq u, \tag{2.23}$$

and rejected otherwise. This process is then repeated for the next sample, starting from $x_{i-1}$ and proposing $x_i$, then accepting or rejecting based on Eq.(2.21).

The *Metropolis* method has the main advantage that it can sample from any distribution, without the requirement of being normalized. However, there are also some disadvantages. To get samples from the desired distribution the process requires many thermalization or "burn-in" steps, to ensure that the sequence of points is not dependent on the initial random sample. It also has the problem that in a high dimensional space, the acceptance rate is small in the case that the full configuration is

changed by a small amount. Therefore, often only a single dimension of the configuration is changed, leading to highly correlated samples.

To overcome these issues, Hamiltonian or Hybrid Monte Carlo (HMC) is introduced. HMC is also a method of MCMC, however, instead of altering the previous configuration with a certain random change, the proposal is based on a molecular dynamics calculation, using Hamiltonian mechanics.

### 2.5.4 Hybrid Monte Carlo

How can we use our knowledge of Hamiltonian mechanics to improve sampling from a distribution? In the previous section we introduced Markov Chain Monte Carlo and the associated Metropolis-Hastings algorithm. In this section we will introduce an improvement on the method by making use of Hamiltonian dynamics. This method is known as Hybrid/Hamiltonian Monte Carlo (HMC) and is a popular method of Monte Carlo integration in which the Markov chain steps are replaced by a molecular dynamics evolution. These dynamical evolutions are related to some Hamiltonian dependent on the desired distribution. Let us first introduce the basis on which this method is build. Just as in MCMC we wish to create a sequence of samples from some probability $p(x)$. In MCMC this sampling is performed by making use of random steps and the Metropolis-Hastings acceptance. In HMC this random step is replaced, and a new proposed point is found through Hamiltonian dynamics instead. With these Hamiltonian dynamics we wish to describe a system of "molecules" which follow a certain potential. To describe the path of these "molecules" we work with a Hamiltonian of the form

$$H = K(\pi) + U(\phi), \tag{2.24}$$

where $K(\pi)$ is the kinetic and $U(\phi)$ potential term. The variables $\pi$ and $\phi$ are the velocity and position of our "molecules" respectively. For the "molecules" to behave such that they move towards the region of higher probability of our distribution, we wish to find a potential which does so. Let us first think of how our particles would behave in a quadratic well (see Fig. 2.5b) In this quadratic

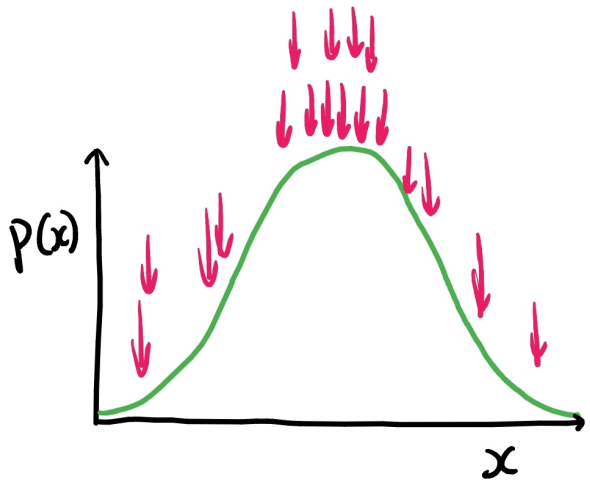


(a) A Gaussian probability distribution, where samples (indicated by red arrows) are taken from the region of higher probability.

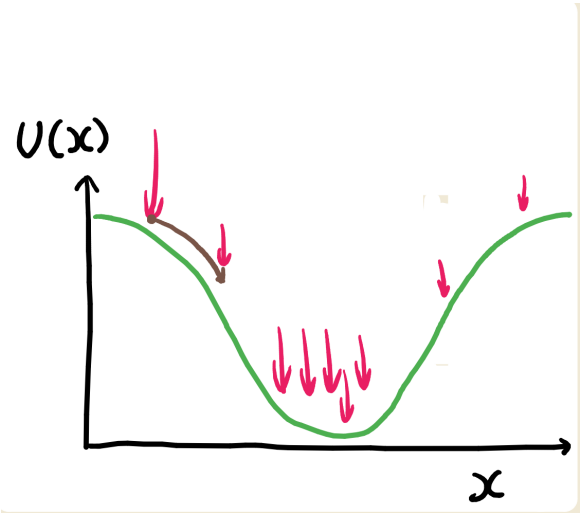


(b) A quadratic well, in which a "molecule" (indicated in brown) flows to the region of the lowest potential.

Figure 2.5: A schematic figure of (a) a quadratic well distribution and (b) the potential well which can be used to describe the classical path moving to the region of lower potential (higher density in the distribution).

well, the "molecules" will slowly flow towards the region of the lowest potential. For the dynamics to sample from our desired distribution, we could introduce a potential as an inverse of the original distribution. Introducing a kinetic energy which acts as a kick to push the "molecules" in a random

direction. For this purpose we can use the general kinetic energy equation

$$K(\pi) = \frac{\pi^2}{2m},$$

with a mass $m$. Now for the potential we will use

$$U(\phi) = -\log\big(p(\phi)\big),$$

where we indeed use the negative function of the desired probability however in logarithmic form. The decision to work with the logarithm comes from the expectation that our distribution scales as a Boltzmann distribution ($p_i \propto e^{-E}$), which is often the case in physics. We then have the joint distribution given by the energy of the Hamiltonian

$$P(\pi, \phi) \propto e^{-E(\pi,\phi)},$$

leading to the distribution

$$\begin{aligned} P(\pi, \phi) &= p(\phi)e^{-\frac{\pi^2}{2m}} \\ &= p(\phi)\mathcal{N}(\pi|0, m), \end{aligned}$$

which is made up of our desired distribution $p$ and a normal distribution $\mathcal{N}(\pi|0, m)$, due to our choice of potential and kinetic term. If we wish to compute the integral

$$\int d\phi g(\phi)p(\phi), \tag{2.25}$$

where $g(\phi)$ is a function and $p(\phi)$ a probability distribution, we can do so by sampling from the joint distribution $P(\pi, \phi)$, as

$$\int d\phi d\pi g(\phi)P(\pi, \phi) = \int d\phi g(\phi)P(\phi) \int d\pi \mathcal{N}(\pi|0, m) = \int d\phi g(\phi)P(\phi). \tag{2.26}$$

How does this allow us to generate samples from the distribution $p(\phi)$? We can do so using Hamiltonian dynamics for which

$$\frac{\mathrm{d}\phi}{\mathrm{d}t} = \frac{\partial \mathcal{H}}{\partial \pi}, \qquad \text{and} \qquad \frac{\mathrm{d}\pi}{\mathrm{d}t} = -\frac{\partial \mathcal{H}}{\partial \phi} \tag{2.27, 2.28}$$

are the partial derivatives describing the "molecule" path. The Hamiltonian dynamics of our "molecules" can be performed through a numerical integrator of partial derivatives such as leap frog integration. With this numerical integrator, a trajectory of length $L$ will be created. The trajectory will take $n$ steps of size $\epsilon$ such that $L = n\epsilon$. The choice of $L$ and $\epsilon$ is important in the computational time of the HMC algorithm. By following this path, our system of $(\pi, \phi)$ moves to a new configuration $(\tilde{\pi}, \tilde{\phi})$. As discussed in section 2.5.3, we require reversibility ($P(x|x') = P(x'|x)$). If we follow a trajectory from $(\pi, \phi) \to (\tilde{\pi}, \tilde{\phi})$ then the probability of this proposal is 1. However, the probability to go back is 0. To satisfy the detailed balance, we should also be able to move from the new configuration $(\tilde{\pi}, \tilde{\phi})$ back to the previous configuration $(\pi, \phi)$. However, following the dynamics, we could not move back to the previous state. We need time reversal for this to occur. Luckily, since the only component dependent on time is $\pi$ and the kinetic term is symmetric in this exchange, we can convert $\tilde{\pi} \to -\tilde{\pi}$ without changing the distribution. From the modified configuration $(-\tilde{\pi}, \tilde{\phi})$ we can move back to $(\pi, \phi)$ satisfying the reversibility.

The choice of integrator is highly important. The error of the integration should be small enough to ensure that there is only a small change in the energy between the initial and final configuration. The integrator must thus be symplectic, ensuring a small error, and time reversible allowing for the detailed balance to be satisfied. Even when an integrator is chosen which is symplectic, it will still produce an error for each path. This error causes the energy of the system to deviate from the original energy, not fully satisfying energy conservation. To overcome this problem, a Metropolis-Hastings

acceptance check is performed after each path. By repeating this process for a large enough number of samples the desired distribution $p(\phi)$ can be approximated.

Now to put it all together in a simple algorithm. The HMC algorithm goes roughly as follows: For each sample

- Compute random momentum $\pi$ from Gaussian distribution with variance given by the momentum mass (pdf: $p(\pi) \propto e^{-\frac{\pi^2}{2m}}$)
- Compute the original Hamiltonian energy ($E = H[\pi, \phi]$)
- Perform the molecular dynamics using an integrator moving the configuration along a path of $n$ steps of size $\epsilon$ with total length $L = n\epsilon$ ($\pi, \phi \to \pi', \phi'$)
- Compute the final Hamiltonian energy ($E' = H[\pi', \phi']$)
- Compute the energy difference for the Metropolis-Hastings check ($\Delta H = E - E'$)
- Perform metropolis check and except or reject configuration with probability ($P = \min(1, e^{-\Delta H})$)

From this algorithm, we can see that, in the ideal case, all samples are accepted. This is the case, because for a symplectic integrator energy is conserved. However, for energy to be conserved, small steps $\epsilon$ should be taken. Since we are aiming to have an efficient algorithm, there is a trade-off in computation time and acceptance rate.

# Chapter 3

# Lattice Field Theory

In this thesis we will be dealing with Graphene by using lattice field theory techniques. Before we will discuss the specifics of a lattice field theory of Graphene, we will describe some relevant attributes of a general lattice field theory. The lattice field theory we are studying is a fermionic field theory.

In many problems, the Hamiltonian can be diagonalized, such that the energy (and thus the relevant probabilities to compute observables) can be obtained. However, in cases where the problem can not simply be diagonalized, approximations have to be made. In this case we will be looking at the path integral formalism which can be used to solve a problem on a discrete lattice. In the limit taking the discrete spacing to zero, this would result in a quantum field theory.

The aim of a lattice field theory is to compute observables $\hat{O}$ through the use of path-integral formalism. The path-integral in which normally the positional spacing $a$ and temporal spacing $\delta t$ are taking to zero, are now kept finite. To obtain the continuum limit results, multiple calculations at finite spacing are then performed and extrapolated to the continuum limits. In the case of Graphene, which has a hexagonal lattice structure, the temporal dimension is discretized and a finite volume of unit cells is used. To extract continuum limit and thermodynamic limit results, both the volume of the system and temporal spacing need to be extrapolated to the continuum and infinite volume.

## 3.1 Path-integral formalism

We wish to look at the equilibrium properties of our system, which are described by the grand-canonical partition function. For a lattice field theory the grand-canonical partition function, $Z = \operatorname{Tr} e^{-\beta H}$, is expressed as a functional integral. This will allow for Monte Carlo Integration to be used. Here the operators in the Hamiltonian have to be replaced by field variables, which can then be stored in a computer. The variable $\beta = 1/k_B T$ is the inverse temperature and is expressed in units of $\mathrm{eV}^{-1}$. Here we will only be dealing with fermionic creation and annihilation operators satisfying the fermionic commutation relations

$$\{a_i^\dagger, a_j^\dagger\} = \{a_i, a_j\} = 0 \text{ and } \quad \{a_i^\dagger, a_j\} = \delta_{ij}. \tag{3.1}$$

We will be using the coherent state functional integral formalism explained in Ref.[20] to compute the partition function $Z$. The quantum mechanical partition function is computed by

$$Z = \sum_n \langle \psi_n | e^{-\beta H} | \psi_n \rangle = \operatorname{Tr} e^{-\beta H}, \tag{3.2}$$

where $|\psi_n\rangle$ denotes the n'th eigenstate of the Hamiltonian. This trace is independent of basis transformation and any complete set can be used to perform the trace. The quantum mechanical partition function obeys the time-dependent Schrödinger equation

$$i\hbar \frac{\partial}{\partial t} |\psi(t)\rangle = \hat{H} |\psi(t)\rangle. \tag{3.3}$$

We can convert the partition function to a system of coherent states given by

$$|\xi\rangle = e^{\sum_\alpha \xi_\alpha a_\alpha^\dagger} |0\rangle \text{ and } \quad \langle \xi| = \langle 0| e^{\sum_\alpha a_\alpha \xi_\alpha^*}, \tag{3.4}$$

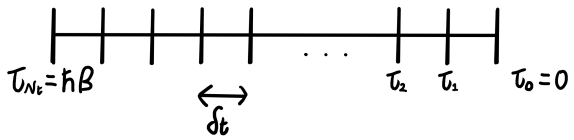


Figure 3.1: Illustration of the slicing of the imaginary-time evolution operator in the interval $[0, \hbar\beta]$ into $N_t$ steps of size $\delta_t$

where the index $\alpha$ labels the spin and position states and the $\xi_\alpha$ are Grassmann-valued fields since we are dealing with fermions. These Grassmann-valued fields obey Grassmann Algebra of which the integration and differentiation rules are described in Ref.[20]. It is also important to note that the coherent states are not orthonormal, but instead obey

$$\langle \xi | \xi' \rangle = e^{\sum_\alpha \xi_\alpha^* \xi'_\alpha}. \tag{3.5}$$

However, the completeness relation of the Fock space of the coherent states is obeyed, so

$$\int \left[ \prod_\alpha d\xi_\alpha^* d\xi_\alpha \right] e^{-\sum_\alpha \xi_\alpha^* \xi_\alpha} |\xi\rangle\langle\xi| = \mathbf{1}, \tag{3.6}$$

where the product and sum run over all single-particle states. In the formalism of these coherent states, the trace of a bosonic operator $\hat{A}$ over the Fock space can be expressed as

$$\mathrm{Tr}\, \hat{A} = \int \left[ \prod_\alpha d\xi_\alpha^* d\xi_\alpha \right] e^{-\sum_\alpha \xi_\alpha^* \xi_\alpha} \langle -\xi | \hat{A} | \xi \rangle, \tag{3.7}$$

where the minus sign in the product comes from the anticommuting nature of Grassmann variables.

To extend Eq.(3.7) to the grand canonical partition function we write

$$Z = \mathrm{Tr}\, e^{-\beta \hat{H}} = \int \left[ \prod_\alpha d\xi_\alpha^* d\xi_\alpha \right] e^{-\sum_\alpha \xi_\alpha^* \xi_\alpha} \langle -\xi | e^{-\beta \hat{H}} | \xi \rangle. \tag{3.8}$$

To calculate the matrix term $\langle -\xi | e^{-\beta \hat{H}} | \xi \rangle$, we first notice that the operator $e^{-\beta \hat{H}}$ is identical to the quantum mechanical time-evolution operator $U(t,0) = e^{-i\frac{t}{\hbar}\hat{H}}$ evaluated at $t = -i\hbar\beta$. We thus wish to solve the imaginary-time evolution operator $U(-i\tau, 0)$ for $\tau = \hbar\beta$. This can be done by splitting the interval $[0, \hbar\beta]$ into $N_t$ identical time slices, where $\tau_j = j\hbar\beta/N_t$ and $j = 0, 1, \ldots, N_t$, such that $\delta t = \hbar\beta/N_t$. By doing so, the matrix product from $\xi_{N_t}$ to $\xi_0$ is given by

$$\langle \xi_{N_t} | e^{-\beta \hat{H}} | \xi_0 \rangle = \int \left( \prod_{j=0}^{N_t - 1} \left[ \prod_\alpha d\xi_{\alpha,j}^* d\xi_{\alpha,j} \right] e^{-\sum_\alpha \xi_{\alpha,j}^* \xi_{\alpha,j}} \right) \prod_{j=0}^{N_t - 1} \langle \xi_{j+1} | e^{-\delta t \hat{H}} | \xi_j \rangle, \tag{3.9}$$

with anti-periodic boundary conditions $\xi_{N_t} = -\xi_0$. These anti-periodic boundary conditions are caused by the anticommuting nature of the Grassmann variables.

Using a small $\delta t$ yields

$$\langle \xi_{j+1} | e^{-\delta t \hat{H}} | \xi_{j-1} \rangle = e^{-\delta t H[\xi_{j+1}^*, \xi_j]} \langle \xi_{j+1} | \xi_j \rangle + \mathcal{O}(\delta t), \tag{3.10}$$

given that $\hat{H}$ is normal ordered. [1] Now using Eq.(3.5) this leads to

$$\langle \xi_{N_t} | e^{-\beta \hat{H}} | \xi_0 \rangle = \int \left( \prod_{j=0}^{N_t - 1} \left[ \prod_\alpha d\xi_{\alpha,j}^* d\xi_{\alpha,j} \right] e^{-\sum_\alpha \xi_{\alpha,j}^* \xi_{\alpha,j}} \right) \prod_{j=0}^{N_t - 1} \exp\left\{ \sum_\alpha \xi_{j+1}^* \xi_j - \delta t H[\xi_{j+1}^*, \xi_j] \right\} + \mathcal{O}(\delta t), \tag{3.11}$$

[1] An operator is normal ordered if all creation operators are to the left of all annihilation operators in the product.

resulting in a partition function

$$\begin{aligned} Z = \operatorname{Tr} e^{-\beta \hat{H}} &= \int \left( \prod_{j=0}^{N_t-1} \left[ \prod_{\alpha} d\xi^*_{\alpha,j} d\xi_{\alpha,j} \right] e^{-\sum_\alpha \xi^*_{\alpha,j}\xi_{\alpha,j}} \right) \prod_{j=0}^{N_t-1} \exp\left\{ \sum_\alpha \xi^*_{j+1}\xi_j - \delta t H[\xi^*_{j+1}, \xi_j] \right\} \\ &= \int \mathcal{D}\xi^* \mathcal{D}\xi \exp\left\{ \sum_{j=0}^{N_t-1} \left[ \sum_\alpha (\xi^*_{\alpha,j+1}\xi_{\alpha,j} - \xi^*_{\alpha,j+1}\xi_{\alpha,j+1}) - \delta t H[\xi^*_{j+1}, \xi_j] \right] \right\} \\ &= \int \mathcal{D}\xi^* \mathcal{D}\xi e^{-S[\xi^*,\xi]}, \end{aligned} \tag{3.12}$$

where we used $\mathcal{D}\xi = \prod_{\alpha,j} d\xi_{\alpha,j}$, and we have the action

$$S[\xi^*, \xi] = \sum_{j=0}^{N_t-1} \left[ \sum_\alpha \xi^*_{\alpha,j+1}(\xi_{\alpha,j+1} - \xi_{\alpha,j}) + \delta t H[\xi^*_{j+1}, \xi_j] \right]. \tag{3.13}$$

In the case that we have an action that is bilinear in the field $\xi$ and $\xi^*$, we can rewrite it in terms of a fermionic matrix $M$

$$S = \sum_{\alpha,\alpha'} \sum_{i,j=0}^{N_t-1} \xi^*_{\alpha,i} M_{(\alpha,i)(\alpha',j)} \xi_{\alpha',j}. \tag{3.14}$$

We can then compute the partition function by performing the integral over the Grassmann-valued fields leading to

$$Z = \int \mathcal{D}\xi^* \mathcal{D}\xi e^{-\sum_{\alpha,\alpha'} \sum_{i,j} \xi^*_{\alpha,i} M_{(\alpha,i)(\alpha',j)} \xi_{\alpha',j}} \propto \det M. \tag{3.15}$$

Using that the integration over a Gaussian integral is given by

$$\int \left[ \prod_{m=1}^{n} d\chi^*_m d\chi_m \right] e^{-\sum_{i,j=1}^n \chi^*_i H_{i,j} \chi_j} \propto [\det H]^{\pm}, \tag{3.16}$$

which holds for both Grassmann variables and complex commuting variables, where a positive sign is set on the right-hand side for Grassmann variables and a negative sign for complex commuting variable. For complex variables, however, the Hamiltonian must be positive Hermitian.
If we only have a bilinear action of fermionic fields, the problem can be solved exactly by making use of Gaussian integrals. However, often interaction terms occur which are 4th order in the creation and annihilation operators. To be able to remove the fermionic degrees of freedom of the theory and perform calculations on the theory, the 4th order terms can be removed by means of a Hubbard-Stratonovich (HS) transformation. The HS transformation does, however, introduce an auxiliary bosonic field $\phi$ which needs to be integrated out. This bosonic field $\phi$ could also have been part of the original theory. This HS auxiliary field $\phi$ will introduce an effective action component $S_{\text{eff}}$ leading to a partition function of the form

$$Z = \int \mathcal{D}\phi \det(M[\phi]) e^{-S_{\text{eff}}[\phi]} \tag{3.17}$$

after integrating out the fermionic degrees of freedom.
To compute the expectation values of an observable in this formalism, we need to solve the integral

$$\langle O \rangle = \int \mathcal{D}\phi O(\phi) \det(M[\phi]) e^{-S_{\text{eff}}[\phi]} = \int \mathcal{D}\phi O(\phi) p(\phi), \tag{3.18}$$

where $O[\phi]$ is a function and $p(\phi)$ the weight associated to the contribution. The function of the observable is obtained by working in the functional formalism of the integral from the operators. The integral of the observable is approximated using Hybrid Monte Carlo integration as explained in chapter 2. To do so, configurations of the $\phi$ field are obtained based on the weight $p(\phi)$, however, this is only possible if it can be considered as a probability distribution, and thus, that $p(\phi) \geq 0$ for all $\phi$.

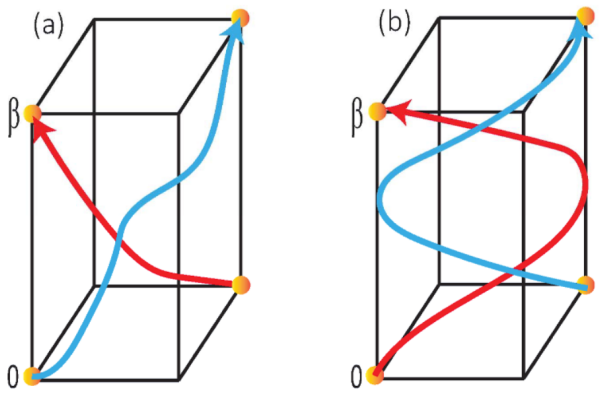


Figure 3.2: Schematic world-line configuration in a $(2+1)$-dimensional space-time lattice taken from Ref.[21]

This is a big problem in performing computations and is known as the sign problem, which will briefly be discussed in the next section. With the set of configurations $\{\phi\}$ containing $N_{conf}$ configuration $\phi$ the integral is then approximated through a sum as

$$\langle O \rangle = \frac{1}{N_{conf}} \sum_{i=1}^{N_{conf}} O(\phi_i) \quad \text{where } \phi_i \in \{\phi\}. \tag{3.19}$$

## 3.2 Sign Problem

One of the major unsolved problems in Quantum Monte Carlo (QMC) methods is that of the numerical sign problem (or fermionic sign problem), often arising in systems of strongly interacting fermions. In the field theory approach described in the previous section, we were dealing with a partition function by using path integral formalism. In general, QMC relies on evaluating the partition function $Z$ by summing over all possible field configurations $c$, weighted by the Boltzmann weight $w(c) = \exp\{-S[c]\}$, with $S[c]$ the action describing the configuration: $Z = \sum_c w(c)$. The configuration in the path-integral formalism, is the world-line in space and imaginary-time of all particles. In Fig.3.2 a schematic world-line configuration is shown.

The main idea of QMC in the path-integral formalism is to perform stochastic samplings of these world-line configurations according to the "probability" $w(c)$. However, in the case of fermionc systems or frustrated bosonic systems, the weights $w(c)$ are not necessarily positive-definite, due to the fermionic nature of the particles. For example, a world-line configuration which has an odd number of fermion exchange leads to a negative Boltzmann weight, as shown in Fig.3.2(a).

As this negative weight can not be treated as a probability, the minus sign causes large issues in the application of QMC. In the case there are no interactions, the fermionic degrees of freedom can usually be integrated out. If 4th order interaction terms appear, the action can be rewritten to remove these interaction terms using an HS transformation, leaving only a Gaussian integral on the fermionic fields and an effective action, as discussed in the previous section. This Gaussian integral can be computed analytically, resulting in a partition function described by a sum over bosonic fields $\phi$. We are thus left with a partition function of the form

$$Z = \int \mathcal{D}\phi p(\phi), \tag{3.20}$$

where $\mathcal{D}\phi$ indicates the measure for the sum over all configuration of $\phi$. The corresponding weight of the different configurations is given by

$$p[\phi] = \det(M(\phi)) e^{-S[\phi]}. \tag{3.21}$$

The action $S[\phi]$ now is the action of the bosonic fields and $M(\phi)$ is a fermionic matrix describing the coupling of the fermions to the $\phi$ field. To compute the expectation value of an observable $O[\phi]$, an

average of the contributions is taken weighted by $p[\phi]$,

$$\langle O \rangle_p = \frac{\int \mathcal{D}\phi O[\phi] p(\phi)}{\int \mathcal{D}\phi p(\phi)}. \tag{3.22}$$

In the case that $p[\phi]$ is positive, it can be interpreted as a probability measure and the techniques of Monte Carlo integration as described in section 2 can be used. In the case that $p[\phi]$ is no longer positive semi-definite, Monte Carlo integration can not be used without additional considerations. The $p[\phi]$ may be negative or even complex, requiring exponential complexity if we wish to obtain the measurements with the same quality compared to simulation without a sign problem.[22] The most straight forward approach to restore stochastic tractability is by reweighing the probability. This is done by treating the complex phase $e^{i\theta}$ of the weight $p[\phi]$ as part of the observable

$$\langle O \rangle_p = \frac{\langle O e^{i\theta} \rangle_{|p|}}{\langle e^{i\theta} \rangle_{|p|}}. \tag{3.23}$$

Adjusting the weights, however, does not solve the sign problem, but only brings it into a different form. The average sign of the Monte Carlo sampling will appear in the denominator, and thus the average will affect how long it will take to obtain accurate results. To achieve a certain accuracy in the measurements of $\langle O \rangle_p$, the number of MC steps increases exponential and equivalently the computation time grows exponentially with the number of particles $N$ and inverse temperature $\beta$.[21] This is known as the *fermion sign problem*. It has been proven that, in general, the fermionic sign problem is nondeterministic polynomial (NP)-hard[23]. This implies that to obtain a general solution of the fermion-sign problem is almost impossible. Most methods which aim to solve the problem are merely methods circumventing the problem by going to a certain basis in which there is no sign problem.

A method to circumvent the sign-problem is by looking at the symmetries of the theory. By using the symmetries to go to a certain basis in which the weight is positive definite, often making use of different fermion flavors. In our particular lattice field theory problem, we will be dealing with a system of two flavors of fermions. Described by the two possible spins: spin up and down. This is what is used in Ref.[24] to circumvent the sign problem and is what we will apply for Graphene, using the particle-hole basis of the theory to create two fermionic matrices which are their complex conjugate. By doing so, we obtain the probability distribution

$$p(\phi) = \det(M(\phi))\det(M^*(\phi))e^{-S[\phi]}, \tag{3.24}$$

for which $\det(M)\det(M^*) = det(MM^\dagger)$ where $MM^\dagger \geq 0$. This is the method that we will apply for our theory of Graphene, utilizing particle-hole symmetry which is present at half-filling.

## 3.3 Limits

The path-integral formalism is well known, analytically the continuum limit is taken in which $\delta t \to 0$, in lattice field theory simulations, however, this is not possible. In lattice field theory, the step size remains finite and a finite number of steps are performed. To investigate a model using lattice field theory, the continuum limit results are often compared to the analytical continuum limit. However, since analytical solutions to models are few and far between, only some can actually be computed in the continuum limit. In LFT, we are working with a lattice and time spacing of a finite number of points. We have a finite volume $V$ and finite lattice spacing. In order to obtain results in a continuum model we need to take two limits

$$V \to \infty, \text{ and } \quad \delta \to 0,$$

the thermodynamic and continuum limit. To do so, we need to run simulations at varying volume $V$ and temporal spacing $\delta t$ in order to perform an extrapolation to these limits. Besides these limits, we will be dealing with an additional limit. In order to be able to compute the inverse of the fermionic matrix, using inversion methods such as the conjugate gradient method, the matrix may not contain

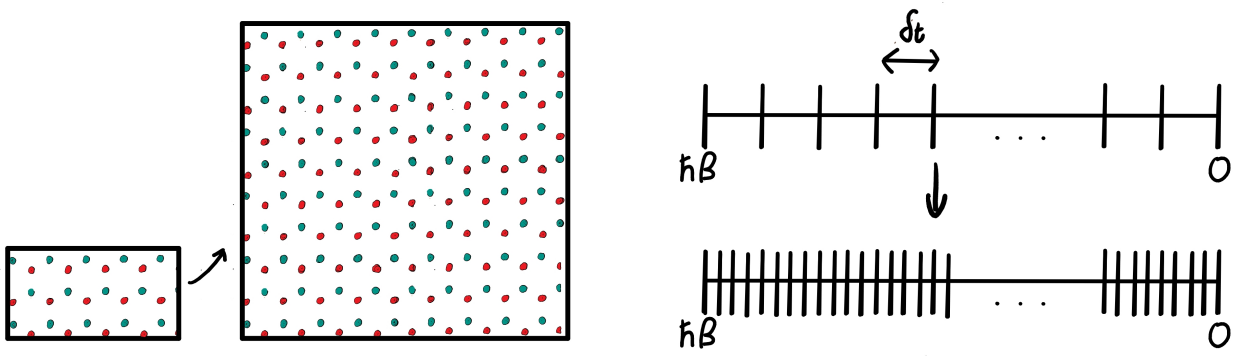


(a) (b)

Figure 3.3: Illustrations of taking the (a) thermodynamic limit $V \to \infty$ and (b) continuum limit$\delta t \to 0$

zero modes. If the matrix contained zero modes the inversion would become extremely hard and require long computation times. To avoid this, a mass term is added to the theory which removes the zero-modes. We then take multiple measurements at varying mass and extrapolate to the limit

$$m \to 0, \tag{3.25}$$

such that the original theory result is obtained.

# Chapter 4

# Graphene

Now that we have described Monte Carlo Integration and the use of Hamiltonian dynamics to obtain samples from a desired distribution, we have given a general idea of lattice field theory and how it may be used to look at systems in the continuum and thermal limit without needing perturbative expansions. We have also shown a mayor issue, which occurs in such methods; the sign problem. In this chapter, we will apply our gained knowledge of lattice field theory, the sign problem and HMC for the Graphene lattice. We will create an effective field theory in 2+1 dimensions which we discretize in time, making an effective lattice field theory of Graphene at finite temperature.

To do so, we will first discuss the Graphene lattice and how this is implemented in our HMC algorithm of Graphene. Next, we will discuss the Hamiltonian which describes Graphene. The Hamiltonian will include a tight-binding (TB) term and Coulomb interaction term. To this we will also add a staggered-mass term, to overcome some computational issues in computing inverses. With the Hamiltonian we will set up a lattice field theory as described in section 3, making specific changes to the method which are relevant for Graphene. With the lattice field theory of Graphene, we will show the necessary steps needed to perform HMC with the model and describe the relevant observables which we will investigate.

This chapter follows the BRS method by Ref.[24]. The BRS method for HMC of Graphene has mostly been applied with Hubbard on-site interactions [11, 25, 26, 27, 3], but studies have also been performed using long-range Coulomb like interactions [24, 8, 28, 5, 29].

## 4.1 Graphene lattice

Graphene is a two-dimensional hexagonal lattice made up of carbon atoms. The unit cell of Graphene contains two sites and the unit cells are oriented in a triangular lattice. This structure can be split into two triangular sublattices as shown in Fig.4.1a where the two sublattices are indicated by red and blue. The two sites in the unit cell are shifted by an inter-atomic lattice spacing $a$. To describe the Graphene structure we will follow the described lattice and basis choice by Ref.[5]. The unit cells which live on a two-dimensional triangular lattice are spanned by the basis vectors

$$\vec{e}_1 = (\sqrt{3}, 0)a \text{ and } \quad \vec{e}_2 = (\tfrac{\sqrt{3}}{2}, \tfrac{3}{2})a. \tag{4.1}$$

With these basis vectors, each lattice point of the triangular lattice can be reached by $\vec{r} = m\vec{e}_1 + n\vec{e}_2$ with $m, n \in \mathbb{N}$. The Hexagonal grid can be constructed from two sets of position vectors $\vec{r}$, both with identical $\{m, n\}$, where one is shifted by $\vec{\delta} = (0, 1)a$. From this construction we can thus see that the hexagonal Graphene lattice is constructed from two triangular sublattices of which one is shifted along $\vec{\delta}$ apart from the other. The two sublattices are referred to as $A$ and $B$.
Since we will be dealing with a system of small finite size, it is good to introduce periodic boundary conditions. The periodic boundary conditions will help reach the infinite volume limit more quickly. If we now restrict $(m, n)$ to $m \in [0, L_m - 1], n \in [0, L_n - 1]$, we obtain a Graphene sheet which is shaped like a parallelogram. To obtain periodic boundary conditions for the simulations we impose

$$(m + L_m, n) \equiv (m, n) \text{ and } \quad (m, n + L_n) \equiv (m - L_n/2, n), \tag{4.2}$$

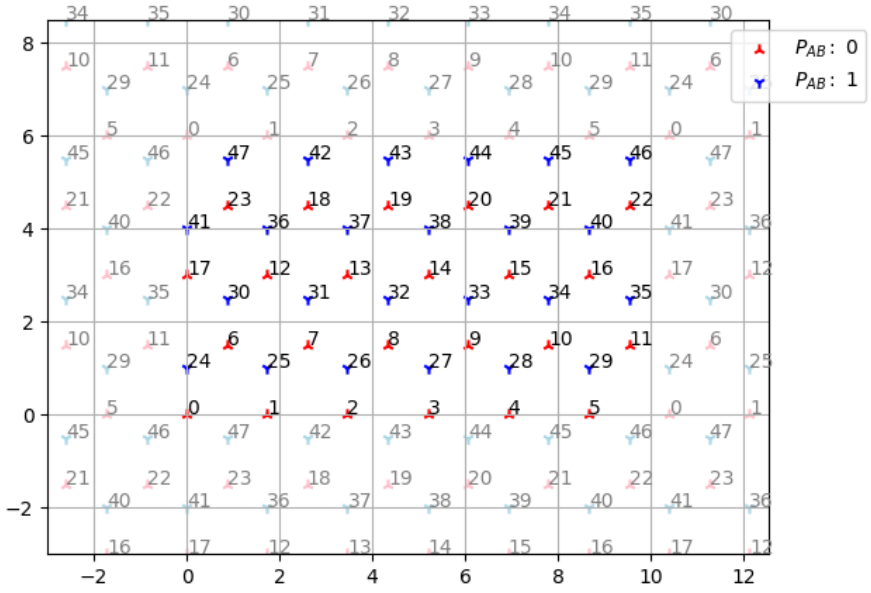


(a) Example figure of the constructed hexagonal lattice with $L_m = 6$ and $L_n = 4$. In the figure the two sublattices can be seen, indicated in either blue or red. The periodic neighbors can also be seen.

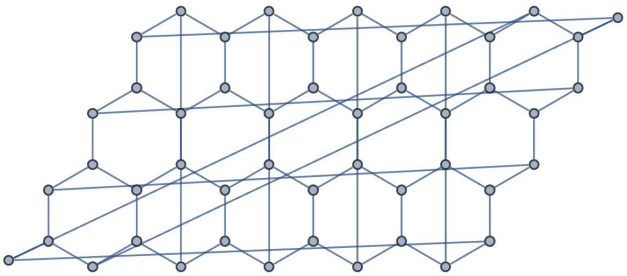

(b) Graph depiction of the lattice with periodic boundary conditions. The top and bottom row of the lattice are connected as neighbors and the left and right sides are connected.

Figure 4.1: (a) The Graphene lattice as used in the simulations with their corresponding index for a lattice of $L_m = 6$ and $L_n = 4$ and (b) a graph description of the periodic boundaries conditions(b)

for which we assumed that $L_m$ and $L_n$ are both even. Since we will be dealing with the Graphene lattice in a lattice field theory, additional euclidean time slice indices ($\tau \in [0, N_t - 1]$) will be introduced. The fields on the lattice sites will be stored on a one dimensional array, where the index for site $m, n$ on sublattice $P_{AB}$ at time slice $\tau$ is given by

$$\text{index} = m + nL_m + \tau(L_m L_n) + P_{AB}(L_m L_n N_t) \tag{4.3}$$

uniquely assigning an index to each lattice site and time. The index is introduced in such a way that all the $A$ sublattice sites (indicated by $P_{AB} = 0$) are counted first and all the $B$ sublattice sites ($P_{AB} = 1$) are counted second. The arrays of the fields will then have a size $D = 2 \times L_m \times L_n \times N_t$ where the two comes from the two sublattices.

## 4.2 Tight-binding Hamiltonian

To describe the properties of Graphene, the tight binding Hamiltonian is used as discussed in section 1.2. This Hamiltonian describes the hopping of electrons from one lattice site to another neighboring site. The tight binding Hamiltonian with spin is written in second quantization as

$$H_{tb} = -\kappa \sum_{\langle x,y \rangle} (a^\dagger_{x,\uparrow} a_{y,\uparrow} + a^\dagger_{x,\downarrow} a_{y,\downarrow} + h.c.), \tag{4.4}$$

in which $\kappa$ is the hopping strength ($\kappa \approx 2.8$eV) and the term $\langle x, y\rangle$ indicates nearest neighbors. For the stability of the simulations, a mass term is added. This mass term is used to remove zero-modes from the model. By removing these zero-modes, the inverse of relevant matrices can be computed in reasonable time. This mass term is given by the Hamiltonian

$$H_m = \sum_x m_x (a^\dagger_{x,\uparrow} a_{x,\uparrow} + a_{x,\downarrow} a^\dagger_{x,\downarrow}), \tag{4.5}$$

where we have a staggered mass $m_x$ which is dependent on which sublattice site $x$ lives,

$$m_x = \begin{cases} +m, & x \in A \\ -m, & x \in B \end{cases}. \tag{4.6}$$

Combining the two Hamiltonian terms leads to a non-interacting Hamiltonian

$$H_0 = H_{tb} + H_m. \tag{4.7}$$

Now introducing interactions we will be looking at a Coulomb type all-to-all interaction, given by the Hamiltonian

$$H_{int} = \frac{1}{2} \sum_{x,y} q_x V_{xy} q_y \tag{4.8}$$

where $q_x = (a^\dagger_{x,\uparrow} a_{x,\uparrow} - a_{x,\downarrow} a^\dagger_{x,\downarrow})$. This interacting term in the Hamiltonian describes the charge interaction and is equivalent to the Hubbard model in the case $V_{xy} = U\delta_{xy}$. However, we will be considering a Coulomb interaction. In section 4.4, the details of the Coulomb interaction will be discussed.

To perform Monte Carlo simulations on a finite lattice field theory, some transformations need to be made to explicitly remove the sign problem. By using that the Hexagonal lattice is a bipartite lattice and that at half-filling (zero chemical potential) the system has a particle hole symmetry, we can rewrite the theory in a basis which does not have a sign problem. We will therefore define the fermionic operators in a particle hole basis as

$$p_x = a_{x,\uparrow}, \quad p^\dagger_x = a^\dagger_{x,\uparrow}, \quad h_x = a^\dagger_{x,\downarrow}, \quad h^\dagger_x = a_{x,\downarrow}, \tag{4.9}$$

which preserves the fermionic commutation relations. In this basis the Tight-binding Hamiltonian can be written as

$$\begin{aligned} H_{tb} &= -\kappa \sum_{\langle x,y\rangle} (a^\dagger_{x,\uparrow} a_{y,\uparrow} + a^\dagger_{x,\downarrow} a_{y,\downarrow} + h.c.) \\ &= -\kappa \sum_{\langle x,y\rangle} (p^\dagger_x p_y + p^\dagger_y p_x + h_x h^\dagger_y + h_y h^\dagger_x) \\ &= -\kappa \sum_{\langle x,y\rangle} (p^\dagger_x p_y + p^\dagger_y p_x - h^\dagger_y h_x - h^\dagger_x h_y), \end{aligned} \tag{4.10}$$

since $\{h^\dagger_x, h_y\} = \delta_{x,y}$. Writing in terms of the particle-hole basis the staggered mass term becomes

$$H_m = m(\sum_{x\in A} - \sum_{x\in B})(p^\dagger_x p_x + h^\dagger_x h_x) = H^{(p)}_m + H^{(h)}_m, \tag{4.11}$$

resulting in two identical terms separating the particle and hole components. The interaction term will convert to

$$H^{(p,h)}_{int} = \frac{1}{2} \sum_{x,y} \tilde{q}_x V_{xy} \tilde{q}_y, \tag{4.12}$$

where now $\tilde{q}_x = (p^\dagger_x p_x - h^\dagger_x h_x)$. To ensure that the particle and hole Hamiltonian components are the same, we can perform a sign flip for the hole operators on one of the two sublattices. So

$$h^\dagger_x \to -h^\dagger_x, \quad h_x \to -h_x \quad \forall\ x \in B, \tag{4.13}$$

which preserves the fermionic anti-commutation relations. The change of sign on one of the sublattices only leads to a change in $H_{tb}$ resulting in

$$H_{tb} = -\kappa \sum_{<x,y>} (p_x^\dagger p_y + p_y^\dagger p_x + h_y h_x^\dagger + h_x h_y^\dagger) = H_{tb}^{(p)} + H_{tb}^{(h)}, \tag{4.14}$$

where we see that we now have two identical Hamiltonian for particles and holes. Adding all the terms together we obtain the full Hamiltonian

$$H = H_{tb}^{(p)} + H_{tb}^{(h)} + H_m^{(p)} + H_m^{(h)} + H_{int}^{(p,h)} = H_0^{(p)} + H_0^{(h)} + H_{int}^{(p,h)}. \tag{4.15}$$

Here we see that the only term connecting the particles and holes is the interaction term.
As discussed in chapter 3, we need a normal ordered form of the Hamiltonian to proceed in creating our lattice field theory of Graphene. The only term requiring additional attention is $H_{int}^{(p,h)}$, where for the off-diagonal term we have the normal ordered form

$$\tilde{q}_x V_{xy} \tilde{q}_y = V_{xy}(-p_x^\dagger p_y^\dagger p_x p_y - p_x^\dagger p_x h_y^\dagger h_y - p_y^\dagger p_y h_x^\dagger h_x - h_x^\dagger h_y^\dagger, h_x h_y) \tag{4.16}$$

and the diagonal terms

$$\tilde{q}_x V_{xx} \tilde{q}_x = -2V_{xx} p_x^\dagger p_x h_x^\dagger h_x + V_{xx}(p_x^\dagger p_x + h_x^\dagger h_x), \tag{4.17}$$

so the interaction in normal ordered form is

$$H_{int}^{(p,h)} =: \tilde{q}_x V_{xy} \tilde{q}_y : + V_{xx}(p_x^\dagger p_x + h_x^\dagger h_x). \tag{4.18}$$

Now that we have obtained a Hamiltonian which is written in normal ordered form, we can go to the path-integral formalism discussed in chapter 3. Before we can continue, however, it is good to notice that we still have quartic term in the Hamiltonian. This term should be removed in order for us to perform a Gaussian integral on the Grassmann valued fields, removing the fermionic degrees of freedom.

## 4.3 Lattice field theory of Graphene

With the Hamiltonian now written in normal ordered form of the particle-hole basis, we can create a lattice field theory. Using coherent states and path-integral formalism, we obtain the grand-canonical partition function

$$Z = \mathrm{Tr}\Big(e^{-\beta H}\Big) = \int \prod_{t=0}^{N_t-1} \Big[ \prod_x d\psi_{x,t}^* d\psi_{x,t} d\eta_{x,t}^* d\eta_{x,t} \Big] e^{-\sum_x (\psi_{x,t+1}^* \psi_{x,t+1} + \eta_{x,t+1}^* \eta_{x,t+1})} \langle \psi_{t+1}, \eta_{t+1} | e^{-\delta H} | \psi_t, \eta_t \rangle. \tag{4.19}$$

We have anti-periodic boundary conditions in time (since we are dealing with fermions),

$$\psi_{x,Nt} = -\psi_{x,0}, \quad \eta_{x,Nt} = -\eta_{x,0}. \tag{4.20}$$

Looking at the matrix $\langle \psi_{t+1}, \eta_{t+1} | e^{-\delta H} | \psi_t, \eta_t \rangle$ and assuming that the Hamiltonian operator is expressed in normal ordered form we can rewrite it as

$$\langle \psi_{t+1}, \eta_{t+1} | e^{-\delta H} | \psi_t, \eta_t \rangle = e^{-\delta H[\psi_{x,t+1}^*, \psi_{x,t}, \eta_{x,t+1}^*, \eta_{x,t}]} e^{\sum_x (\psi_{x,t+1}^* \psi_{x,t} + \eta_{x,t+1}^* \eta_{x,t})}, \tag{4.21}$$

which introduces a discretization error of order $\mathcal{O}(\delta t)$. Filling in our normal ordered Hamiltonian in the discrete action Eq.(3.13) with two fields, we have

$$\begin{aligned} S[\psi^*, \psi, \eta^*, \eta] = \sum_t \Big[ &- \sum_x \psi_{x,t+1}^* (\psi_{x,t} - \psi_{x,t+1}) - \sum_x \eta_{x,t+1}^* (\eta_{x,t} - \eta_{x,t+1}) \\ &+ \delta t \big( H_0^{(p)}[\psi^*, \psi] + H_0^{(h)}[\eta^*, \eta] + \frac{1}{2} \sum_{x,y} Q_{x,t} V_{x,y} Q_{y,t} + \sum_x V_{xx} (\psi_{x,t+1}^* \psi_{x,t} + \eta_{x,t+1}^* \eta_{x,t}) \big) \Big], \end{aligned} \tag{4.22}$$

with $Q_{x,t} = \psi^*_{x,t+1}\psi_{x,t} - \eta^*_{x,t+1}\eta_{x,t}$. To remove the interaction term, which is of fourth power in the Grassmann fields, we need to perform a Hubbard Stratonovich transformation, introducing an auxiliary field $\phi$,

$$e^{-\frac{\delta}{2}\sum_t \sum_{x,y} Q_{x,t}V_{x,y}Q_{y,t}} \propto \int \mathcal{D}\phi \exp\left\{ -\sum_{x,y}\sum_t \phi_{x,t}V^{-1}x,y\phi_{y,t} - i\delta\sum_t \phi_{x,t}Q_{x,t} \right\}. \tag{4.23}$$

In appendix B,S a general derivation of the above transformation is given. The specific choice to use a complex transformation of the gaussian integral term, is to ensure that the fermionic matrices which are generated by the two fields are their conjugate. In this manner, the square of these matrices will be real positive semi-definite. If another choice of HS transformation was made (e.g. a shift along the Real axis), this would not be the case, resulting in a sign problem. Applying the HS transformation, we obtain the partition function

$$\begin{aligned} \mathrm{Tr}\left(e^{-\beta H}\right) &= \int \mathcal{D}\psi\mathcal{D}\psi^*\mathcal{D}\eta\mathcal{D}\eta^*\mathcal{D}\phi \exp\Big\{ -\frac{\delta}{2}\sum_{t=0}^{N_t-1}\sum_{x,y}\phi_{x,t}V^{-1}_{x,y}\phi_{y,t} \\ &\quad - \sum_{t,t'=0}^{N_t-1}\sum_{x,x'}\left[\psi^*_{x,t}M_{(x,t)(x',t')}\psi_{x',t'} + \eta^*_{x,t}M^*_{(x,t)(x',t')}\eta_{x',t'}\right]\Big\} \\ &= \int \mathcal{D}\psi\mathcal{D}\psi^*\mathcal{D}\eta\mathcal{D}\eta^*\mathcal{D}\phi \exp\Big\{ -S_{\mathrm{eff}}[\phi] - S_M[\psi^*,\psi] - S_{M^*}[\eta^*,\eta]\Big\}, \end{aligned} \tag{4.24}$$

with

$$\begin{aligned} M_{(x,t)(y,t')} =& \delta_{x,y}(\delta_{t,t'} - \delta_{t-1,t'}) - \kappa\frac{\beta}{N_t}\sum_n \delta_{y,x+n}\delta_{t-1,t'} + m_x\frac{\beta}{Nt}\delta_{x,y}\delta_{t-1,t'} \\ &+ \frac{V_{xx}}{2}\frac{\beta}{N_t}\delta_{x,y}\delta_{t-1,t'} + i\phi_{x,t}\frac{\beta}{N_t}\delta_{x,y}\delta_{t-1,t'}. \end{aligned} \tag{4.25}$$

The fermionic matrix $M$ of the particle field $\psi$ and the complex conjugate of this matrix $M^*$ is the fermionic matrix of the hole field $\eta$. $M$ is written in the linear discretization form described in Ref.[7]. To remove the Grassmann valued fields of the fermions, we apply a Gaussian integral on the fermionic fields. By doing so we obtain

$$\begin{aligned} \mathrm{Tr}\left(e^{-\beta H}\right) &= \int \mathcal{D}\phi \mathrm{det}(M^*(\phi))\mathrm{det}(M(\phi)) \exp\left\{ -\frac{\delta}{2}\sum_{t=0}^{N_t-1}\sum_{x,y}\phi_{x,t}V^{-1}x,y\phi_{y,t} \right\} \\ &= \int \mathcal{D}\phi \mathrm{det}(M(\phi)M^\dagger(\phi)) \exp\left\{ -\frac{\delta}{2}\sum_{t=0}^{N_t-1}\sum_{x,y}\phi_{x,t}V^{-1}x,y\phi_{y,t} \right\}. \end{aligned} \tag{4.26}$$

We can now see that the use of the particle hole symmetry and our choice of HS transformation has lead to a real determinant of the square matrices. Since the fermionic matrix is symmetric in particle and holes, with the only distinction in the matrices being the imaginary contribution of the HS field $\phi$. One important problem that arises with fermionic matrix eq.(4.25) is that the determinant will contain powers of the $\phi$ field up to $\phi^N$, with $N$ the number of lattice sites. This is a problem, since the $\phi$ field is non-compact. This causes numerical instabilities due to the amplification of rounding errors for which the solution was found in Ref.[30]. The solution is to replace

$$-\delta_{xy}\delta_{t-1,t'} + \frac{\beta}{N_t}\frac{V_{xx}}{2}\delta_{xy}\delta_{t-1,t'} + i\frac{\beta}{N_t}\phi_{x,t}\delta_{xy}\delta_{t-1,t'} \to -e^{-i\frac{\beta}{N_t}\phi_{x,t}}\delta_{xy}\delta_{t-1,t'}, \tag{4.27}$$

which introduces a compact-link field making the determinant numerically stable, as it now contains sums over $\phi$ instead of products. This is an appropriate transformation because in the temporal

continuum limit $\delta t \to 0$ the action in Eq.(4.24) becomes invariant under spatially constant one-dimensional (temporal) gauge transformations[8]. This results in the fermionic matrix

$$M_{(x,t)(y,t')} = \delta_{x,y}(\delta_{t,t'} - e^{-i\frac{\beta}{N_t}\phi_{x,t}}\delta_{t-1,t'}) - \kappa\frac{\beta}{N_t}\sum_n \delta_{y,x+n}\delta_{t-1,t'} + m_x\frac{\beta}{Nt}\delta_{x,y}\delta_{t-1,t'}. \tag{4.28}$$

We can see that in the limit $\delta t \to 0$, the two different representations of the fermionic matrix lead to the same continuum theory.

## 4.4 Coulomb potential

We will be looking at the Graphene lattice in an interacting theory. One of the most important attributes to the theory of Graphene is the inter-atomic interaction. The term moving the system away from the non-interacting system of the tight-binding model with simple electron hopping, and into a more complex system of strong-interactions. The interaction term, containing the interaction matrix $V$, is found in the HS effective action as

$$S_{\text{eff}}(\phi) = \frac{\delta}{2}\sum_{t=0}^{N_t-1}\sum_{x,y}\phi_{x,t}V_{xy}^{-1}\phi_{y,t}. \tag{4.29}$$

The interaction matrix $V$ contains both the potential and natural unit factors. We will be looking at a Coulomb type interaction for the two-body potential. The potential will depend only on the distance between the two lattice sites, thus, we have

$$V_{xy} = V(x_1 - y_1, x_2 - y_2) \equiv V(r), \tag{4.30}$$

where $r$ is the distance between two lattice sites. The most straightforward choice for the potential would be the standard Coulomb potential,

$$V(r) = \frac{e^2}{r}, \tag{4.31}$$

where $e^2$ is the coupling constant ($e^2 \approx 1/137$). A short distance cut off would be added at $r_0 = 0.5a$ and the on-site interaction set to $V_{xx} = 1/(r_0 a)$. The standard Coulomb potential was used in Ref.[24, 8] for the HMC calculations of Graphene. The standard Coulomb potential is, however, insufficient to account for the short-distance screening by the electrons in the $\sigma$-bands of Graphene and other higher energy states[5].
In our measurements we use the partialy screened Coulomb interaction used in Ref.[5]. This interaction potential uses results from Ref.[12], where the screening was investigated within a constrained random phase approximation (cRPA). The results obtained by this technique for the on-site ($V_{xy} = U_{00}$ with $r_{xy} = |x - y| = 0$), nearest-neighbor ($V_{xy} = U_{01}$ with $r_{xy} = a$), next-nearest-neighbor ($V_{xy} = U_{02}$ with $r_{xy} = \sqrt{3}a$) and third-nearest-neighbor ($V_{xy} = U_{03}$ with $r_{xy} = 2a$) have been used as the interaction strength at short distance. The values for the different strengths found using the cRPA calculations are shown in the table below.

| | $U_{00}$ (eV) | $U_{01}$ (eV) | $U_{02}$ (eV) | $U_{03}$ (eV) |
|---|---|---|---|---|
| cRPA | 9.3 | 5.5 | 4.1 | 3.6 |

This short-distance screening was previously implemented in Ref.[11], which assumed that the potential decays roughly as $1/(\epsilon_\sigma r)$ at longer distance, where the constant $\epsilon_\sigma = 1.41$ was adjusted to match the third-nearest-neighbor term at $r = 2a$ to $V(2a) = U_{03}$. Alternatively, to describe the screening from the $\sigma$-bands and other localized electrons, a piece-wise potential was introduced in Ref.[5], having a decay function with different parameters dependent on the length scale. The function for the partially screened potential was determined by performing an inverse Fourier transform of the unscreened coulomb potential, with a phenomenological dielectric screening function added to the

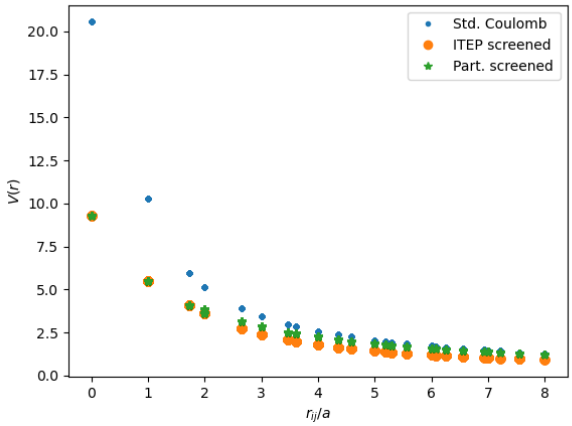


Figure 4.2: Graph of the three different Coulomb type potentials as a function of distance on the hexagonal Graphene lattice. The Standard Coulomb, "ITEP screened potential" (with $1/\epsilon_\sigma r$ decay after the cRPA pionts), and the Partially screened potential (using the piece-wise potential Eq.(4.32))

unscreened potential and parameterized for computational efficiency. This potential then connects the explicit short-distance screening with the screened long-wavelength limits. To efficiently perform the computations, this screened potential is parameterized into an exponential Ansatz, which assumes exponential screening[5]. The resulting piece-wise defined potential is

$$V(r) = \begin{cases} U_{00}, U_{01}, U_{02}, U_{03} & , \ r \leq 2a \\ e^2(m_0[e^{-m_2 r}/(m_1 r)^\gamma] + m_3) & , \ r > 2a, \end{cases} \tag{4.32}$$

where $a$ is the lattice spacing, $m_1 = 1\text{eV}$ and the parameters $m_0$, $m_2$, $m_3$, $\gamma$ differ depending on the length-scale. In Ref.[5], the parameters of the piece-wise screened potential can be found. In Fig.4.2, the three different potentials described are shown, the Standard Coulomb and "ITEP screened potential" (with $1/\epsilon_\sigma r$ decay after the cRPA pionts), and the Partially screened potential (using the piece-wise potential Eq.(4.32)). In order to account for system size, the potential was implemented taking periodic boundary conditions into account. For any two points $x$ and $y$ on the lattice, we determine the shortest path between these points allowing for boundary crossings. In our measurements we will look at the dependency of the order-parameters of the system on the interaction strength. We do this by scaling the potential by $V = V/\epsilon$ with $\epsilon = (300/137)/\alpha_{\text{eff}}$. We will discuss our results in terms of $\alpha_{\text{eff}}$, the *effective* fine-structure constant.

## 4.5 Hybrid Monte Carlo for Graphene

We now have a lattice field theory partition function, independent of a sign problem, which can therefore be used to compute observables. How do we now compute the observables of the system?

We do this by the use of Hybrid Monte Carlo integration, as explained in chapter 2.5.4, to compute observables as

$$\langle \mathcal{O}_1(t_1)\mathcal{O}_2(t_2)\ldots\rangle = \frac{1}{Z}\,\mathrm{Tr}\Big(T[\mathcal{O}_1(t_1)\mathcal{O}_2(t_2)\ldots]e^{-\beta H}\Big). \tag{4.33}$$

Which in the path-integral formalism described can be done through an integral

$$\langle O\rangle = \int \mathcal{D}\phi O(\phi)P(\phi), \tag{4.34}$$

where

$$P(\phi) = \frac{1}{Z}\det(M(\phi)M^\dagger(\phi))e^{-S_{\text{eff}}[\phi]}. \tag{4.35}$$

Here $\phi$ is the auxiliary HS field introduced in the previous section, $O(\phi)$ is a function of the field describing the observable, with $S_{\text{eff}}[\phi]$ the remaining part of the action dependent on $\phi$ and $\det(M(\phi)M^\dagger(\phi))$

accounting for the fermionic effects. The Monte Carlo approach to this problem is to generate configurations of $\phi$ such that the integral over the auxiliary field can be approximated. These configurations are obtained using the HMC algorithm as described in chapter 2.5.4. However, the fermionic determinants can not simply be determent each configuration, as this would be to computationally expensive. Instead, we represent the fermion determinants as a gaussian integral over psuedofermionic fields $\chi$. The $\chi$ are complex commuting fields rather than Grassmann valued such that

$$\det(MM^\dagger) = \int \mathcal{D}\chi\mathcal{D}\chi^* e^{-\sum_{t,t'=0}^{N_t-1}\sum_{x,x'}\chi^*_{x,t}(MM^\dagger)^{-1}\chi_{x',t'}}, \tag{4.36}$$

using Eq.(3.16), with negative sign on the rhs (i.e. complex commuting fields, bosonic fields). This leads to the partition function as

$$\mathrm{Tr}\Big(e^{-\beta H}\Big) = \int \mathcal{D}\phi\mathcal{D}\chi\mathcal{D}\chi^* P(\phi,\chi,\chi^*), \tag{4.37}$$

with

$$P(\phi,\chi,\chi^*) = \exp\left\{-\frac{\delta}{2}\sum_{t=0}^{N_t-1}\sum_{x,y}\phi_{x,t}V^{-1}_{xy}\phi_{y,t} - \sum_{t,t'=0}^{N_t-1}\sum_{x,x'}\chi^*_{x,t}(MM^\dagger)^{-1}\chi_{x',t'}\right\}, \tag{4.38}$$

a distribution dependent both on $\phi$ and our psuedofermionic fields $\chi^*, \chi$. To approach this, we sample $\phi$ and $\chi$ separately: we can generate $P(\chi) \sim e^{-\chi^\dagger(MM^\dagger)^{-1}\chi}$ directly as a Gaussian and perform a molecular dynamics evolution for the $\phi$ field, introducing a fictitious momentum field $\pi$. To sample the $\chi$ field, we will sample $\rho$ from a Gaussian distribution,

$$P(\rho) \sim e^{-\rho^\dagger\rho}, \tag{4.39}$$

and obtain $\chi = M\rho$ from this $\rho$. The real fictitious momentum field $\pi$ is sampled from a Gaussian distribution, for which we have taken unit variance $P(\pi) \sim e^{-\pi^2/2}$ and the HS field $\phi$ is obtained by evolving the $\phi$ and $\pi$ using Hamiltonian dynamics. We thus have the Hamiltonian describing the dynamics

$$\mathcal{H} = -\mathrm{Ln}[P(\phi;\chi,\chi^*)] = \frac{\delta t}{2}\sum_{t=0}^{N_t-1}\sum_{x,y}\phi_{x,t}V^{-1}_{xy}\phi_{y,t} + \sum_{t,t'=0}^{N_t-1}\sum_{x,x'}\chi^*_{x,t}(MM^\dagger)^{-1}\chi_{x',t'} + \frac{1}{2}\sum_{t=0}^{N_t-1}\sum_{x}\pi^2_{x,t}, \tag{4.40}$$

which we will write in matrix notation as

$$\mathcal{H} = \frac{\delta t}{2}\phi^T V^{-1}\phi + \chi^\dagger(MM^\dagger)^{-1}\chi + \frac{\pi^T\pi}{2}. \tag{4.41}$$

The partial derivatives needed to compute the evolution, as discussed in chapter 2.5.4, are found to be

$$\left[\frac{d\phi}{d\tau}\right]^T = \frac{\partial\mathcal{H}}{\partial\pi} = \pi^T, \tag{4.42}$$

and

$$\left[\frac{d\pi}{d\tau}\right]^T = -\frac{\partial\mathcal{H}}{\partial\phi} = -\delta\phi^T V^{-1} - \frac{\partial}{\partial\phi}[\chi^\dagger(MM^\dagger)^{-1}\chi] \equiv F_\phi + F_\chi. \tag{4.43}$$

[5] With the $F_\phi$ component given by

$$F_\phi = -\delta\phi^T V^{-1}, \tag{4.44}$$

and the $F_\chi$ component by

$$(F_\chi)_i = -\frac{\partial}{\partial\phi}[\chi^\dagger(MM^\dagger)^{-1}\chi] = 2\mathrm{Re}[\eta^\dagger\frac{\partial M}{\partial\phi_i}\xi], \tag{4.45}$$

for a given component $i = (x,t)$. Here we have introduced

$$\eta = (MM^\dagger)^{-1}\chi \text{ and } \quad \xi = M^{-1} = M^\dagger\eta, \tag{4.46}$$

which will be extremely useful in our computations, as we can compute the $\eta$ by applying the conjugate gradient method, since $MM^\dagger$ is positive Hermitian and $\chi$ a complex source vector. [1] We can then compute $\xi$ by multiplying $\eta$ with $M^\dagger$. The conjugate gradient method uses minimization techniques to compute

$$y = A^{-1}x, \tag{4.47}$$

for a positive Hermitian matrix $A$ and a complex source vector $x$. It uses these minimization techniques to determine the $y$, minimizing such that

$$Ay = x. \tag{4.48}$$

As described in the previous section, we have two possible fermionic matrices, for these two matrices we have that the resulting fermionic matrix component to the partial derivative is

$$(F_\chi)_i = -2\frac{\beta}{N_t}\mathrm{Im}[\eta^*_{(x,t)}\xi_{x,t-1}], \tag{4.49}$$

for eq.(4.25)[5], and

$$(F_\chi)_i = -2\frac{\beta}{N_t}\mathrm{Im}[\eta^*_{(x,t)}e^{-i\frac{\beta}{N_t}\phi_{x,t}}\xi_{(x,t-1)}], \tag{4.50}$$

for eq.(4.28)[5]. Since our partial derivative is split into two separate component, the Sexton-Weingarten integrator[32], discussed in appendix A, can be used. This integrator performs $m_{sw}$ small steps of $\epsilon/m_{sw}$ on one of the components, and a single large step $\epsilon$ on the other. By doing so, it improves the accuracy and therefore number of steps $n$ and step-size $\epsilon$ required.
The complete HMC algorithm is then constructed by repeating the following steps:

- Update the momentum field $\pi$ using Gaussian noise: $P(\pi) \sim e^{-\pi^2/2}$
- Update the psuedofermionic field $\chi$ by generating a complex field $\rho$ using a complex gaussian distribution $P(\rho) \sim e^{-\rho^\dagger\rho}$ and computing $\chi = M\rho$ from this
- Compute the original Hamiltonian energy ($E = \mathcal{H}[\phi, \pi, \chi, \chi^*]$)
- Generate a molecular dynamics trajectory by performing integration steps following the Hamiltonian given by eq.(4.41). The integration takes a path of $n$ steps of length $\epsilon$ for a total length of $L = n\epsilon$ in the trajectory time. ($\pi, \phi \to \pi', \phi'$)
- Compute the final Hamiltonian energy ($E' = \mathcal{H}[\phi', \pi', \chi, \chi^*]$) and compute the energy difference ($\Delta H = E - E'$)
- Perform metropolis check and accept or reject configuration with probability $P = \min(1, e^{-\Delta H})$.

By proceeding these steps, we generate a set of configuration $\{\phi\}$ with which the observables can be computed.

## 4.6 Observables

With the configurations $\{\phi\}$ obtained using the HMC algorithm described in the previous section, we can start looking at the observables which describe sublattice symmetry breaking. What are the observable which quantify this symmetry breaking?

Sublattice symmetry can be quantified by looking at the difference in spin between the two sublattices. In the case the system obeys sublattice symmetry, the average spin on both sublattices will be equal, and thus give a difference of zero. When this symmetry is broken, the sublattice spin difference would give non-zero results. We will be looking at one-point and two-point functions of local spin operators, as described by Ref.[27]. The observables are described by a spin operator given by

$$S^i_x = \frac{1}{2}(a^\dagger_{x,\uparrow}, a^\dagger_{x,\downarrow})\sigma^i(a_{x,\uparrow}, a_{x,\downarrow})^T, \tag{4.51}$$

[1] In Ref.[31], a description of the conjugate gradient method is given.

where $\sigma^i$ is the $i$th Pauli matrix. Now going to the particle hole basis with a change of sign on the hole-operator in one of the sublattices, as described in chapter 4.2, we get

$$S_x^i = \frac{1}{2}(p_x^\dagger, A_x h_x)\sigma^i(p_x, A_x h_x^\dagger)^T, \tag{4.52}$$

with

$$A_x = \begin{cases} 1 & \text{if } x \in A \\ -1 & \text{if } x \in B, \end{cases} \tag{4.53}$$

where the sign dependents on the sublattice. During our measurements, we will be looking at the spin in the $z$ direction with corresponding Pauli matrix,

$$\sigma^3 = \begin{pmatrix} 1 & 0 \\ 0 & -1, \end{pmatrix} \tag{4.54}$$

which gives the spin operator

$$S_x^3 = \frac{1}{2}(p_x^\dagger p_x - h_x h_x^\dagger). \tag{4.55}$$

We will be looking at sublattice symmetry breaking, which corresponds to an antiferromagnetic term. In the case we were to look a ferromagnetic behavior, we would consider the uniform magnetization as

$$S_+^i = \sum_x^N S_x^i, \tag{4.56}$$

summing the spins coherently. We are however interested in the antiferromagnetic behavior, which has a staggered magnetization

$$S_-^i = \sum_x^N A_x S_x^i, \tag{4.57}$$

computing the difference between the sublattices.
The two-point function we will be looking at is

$$S_{--}^{33} = \langle\langle S_-^3 S_-^3 \rangle\rangle, \tag{4.58}$$

where we use the expectation value of two operators

$$\langle\langle \mathcal{O}_1 \mathcal{O}_2 \rangle\rangle = \langle \mathcal{O}_1 \mathcal{O}_2 \rangle - \langle \mathcal{O}_1 \rangle \langle \mathcal{O}_2 \rangle. \tag{4.59}$$

Since we are working at half-filling and thus the number of particles and holes are the same, we expect that the extensive one-point function $\langle S_-^3 \rangle$ vanishes for all $\alpha_{\text{eff}}$. We, therefore, have that the two-point function is expected to simply become

$$S_{--}^{33} = \langle S_-^3 S_-^3 \rangle. \tag{4.60}$$

To compute the observables, we will add source terms to our theory, starting from the partition function Eq.(4.24). We add the source terms $-\psi^* \cdot J - J^* \cdot \psi$ to the action, for both fermionic fields using $J$ for the particle field $\psi$ and $g$ for the hole field $\eta$. The partition function, with added source terms, is given by

$$\begin{aligned} Z[j, j^*, g^*, g] = \int \mathcal{D}\psi \mathcal{D}\psi^* \mathcal{D}\eta \mathcal{D}\eta^* \mathcal{D}\phi \, \exp\Big\{ & - S_{\text{eff}}[\phi] - S_M[\psi^*, \psi] - S_{M^*}[\eta^*, \eta] \\ & + \psi^* \cdot J + J^* \cdot \psi + \eta^* \cdot g + g^* \cdot \eta - J^* \cdot M^{-1} J - g^* \cdot M^{*-1} g \Big\}, \end{aligned} \tag{4.61}$$

where we used vector/matrix notation and $\cdot$ the dot product between two vectors. We rewrite the observable into a functional form by differentiating with respect to these source terms. For example, the particle correlator $\langle p_{x,\tau} p^\dagger_{y,0}\rangle$ is computed as

$$\begin{aligned}\langle p_{x,\tau} p^\dagger_{y,0}\rangle =& \int \mathcal{D}\psi\mathcal{D}\psi^*\mathcal{D}\eta\mathcal{D}\eta^*\mathcal{D}\phi\ \psi_{x,t}\psi^*_{y,0}\ e^{-S} \\ =& \frac{1}{Z[0,0,0,0]}\frac{\delta^2}{\delta J^*_{x,\tau}\delta J_{y,0}} Z[J,J^*,0,0]\Big|_{J=0} \\ =& M^{-1}_{(x,\tau)(y,0)}.\end{aligned} \tag{4.62}$$

During the simulations, most measurements have been performed on the sublattice spin difference $S^3_-$, however, to look for a phase transition the antiferromagnetic spin density wave $\langle S^{33}_{--}\rangle$ was also considered. We can obtain the functional form of $\langle S^3_-\rangle$ from the lattice field theory in two manners, either by introducing source terms as described above or by using the mass term as an effective source term. The observable $S^3_-$ can be written in normal-ordered for as

$$\begin{aligned}S^3_- =& \sum_x A_x S^3_x \\ =& \sum_x A_x (p^\dagger_x p_x - h_x h^\dagger_x) \\ =& \sum_x A_x (p^\dagger_x p_x + h^\dagger_x h_x - 1) \\ =& \sum_x A_x (p^\dagger_x p_x + h^\dagger_x h_x),\end{aligned} \tag{4.63}$$

since the number of sites $N_A = N_B$ cancels the $-1$. $S^3_-$ computes the spin difference between the two sublattices. Computing the observable using Monte Carlo integration we have

$$\langle S^3_-\rangle = \sum_{x\in\{A\}} \langle p^\dagger_x p_x + h^\dagger_x h_x\rangle - \sum_{x\in\{B\}} \langle p^\dagger_x p_x + h^\dagger_x h_x\rangle, \tag{4.64}$$

which in the path-integral formalism leads to,

$$\begin{aligned}\langle S^3_-\rangle =& \frac{1}{ZN_t}\int \mathcal{D}\psi^*\mathcal{D}\psi\mathcal{D}\eta^*\mathcal{D}\eta\mathcal{D}\phi \Big\{ \sum_{x\in\{A\},t} \psi^*_{x,t+1}\psi_{x,t} + \eta^*_{x,t+1}\eta_{x,t} - \sum_{x\in\{B\},t} \psi^*_{x,t+1}\psi_{x,t} + \eta^*_{x,t+1}\eta_{x,t}\Big\} \\ & \times \exp\Big\{ -(\psi^*|M|\psi) - (\eta^*|M^*|\eta) - S_{\text{eff}}[\phi]\Big\}.\end{aligned} \tag{4.65}$$

The staggered mass term Eq.(4.11) can act as a source term to the sublattice spin difference. Therefore, we can compute the sublattice spin difference as

$$\langle S^3_-\rangle = -\partial_m Z. \tag{4.66}$$

By performing the derivative, we obtain

$$\begin{aligned}\langle S^3_-\rangle =& \frac{-1}{ZN_t}\int \prod_{t=0}^{N_t-1}\Big[\prod_x d\psi^*_{x,t} d\psi_{x,t} d\eta^*_{x,t} d\eta_{x,t}\Big]\partial_m e^{-(\psi^*|M|\psi)-(\eta^*|M^*|\eta)-S_{\text{eff}}[\phi]} \\ =& \frac{-1}{ZNt}\int \mathcal{D}\phi\partial_m(Det(M)Det(M^*))e^{-S_{\text{eff}}[\phi]} \\ =& \frac{-1}{ZNt}\int \mathcal{D}\phi Det(M)Det(M^*)(\text{Tr}\left[M^{-1}\frac{\partial M}{\partial m}\right] + Tr\left[M^{*,-1}\frac{\partial M^*}{\partial m}\right])e^{-S_{\text{eff}}[\phi]} \\ =& \frac{-2}{ZNt}\int \mathcal{D}\phi Det(M)Det(M^*)Re(Tr\left[M^{-1}\frac{\partial M}{\partial m}\right])e^{-S_{\text{eff}}[\phi]} \\ =& \frac{-2}{Nt}\int \mathcal{D}\phi Re(Tr\left[M^{-1}\frac{\partial M}{\partial m}\right])e^{-S_{\text{eff}}[\phi]}\end{aligned} \tag{4.67}$$

using Jacobi's formula for the derivative of a determinant. We also used that $a + a^* = 2Re(a)$. The derivative to fermionic matrix Eq.(4.25) and Eq.(4.28) is

$$\frac{\partial M_{(x,t)(y,t')}}{\partial m} = A_x \frac{\beta}{Nt} \delta_{x,y} \delta_{t-1,t'}, \tag{4.68}$$

where we used $A_x$ to describe the staggered mass being $+1$ on the A lattice and $-1$ on the $B$ lattices. The observable can thus be computed using Monte Carlo integration, with configurations $\{\phi\}$ as

$$\langle S^3_- \rangle = \frac{-2}{N_t N_{conf}} \sum_{\phi} \mathrm{Re} \left\{ \sum_{t=0}^{N_t - 1} \sum_x A_x M^{-1}_{(x,t)(x,t+1)} \right\}. \tag{4.69}$$

If we were to perform the derivation by using the added source terms shown in Eq.(4.65), we would get the same result.

For the two-point correlator of spins in the $z$ direction $S^{33}_{--}$ we have

$$\begin{aligned} S^{33}_{--} =& S^3_- S^3_- \\ =& (\sum_x^N A_x s^3_x)(\sum_y^N A_y s^3_y) \\ =& \frac{1}{4} \left( \sum_{x,y}^N A_x A_y (p^\dagger_x p_x - h_x h^\dagger_x)(p^\dagger_y p_y - h_y h^\dagger_y) \right). \end{aligned} \tag{4.70}$$

We can split the sum over the lattice sites $x$ and $y$ into two types, $(x \sim y)$ and $(x \nsim y)$ indicating $x$ and $y$ being on the same or different sublattice, respectively. We thus have 8 different types of components in the observable, 4 different quartic operators each occurring twice, once with $(x \sim y)$ and once with $(x \nsim y)$. The different components and their normal ordered form are given by

$$p^\dagger_x p_x p^\dagger_y p_y = \begin{cases} -p_x p_y p^\dagger_x p^\dagger_y + p_x \delta_{x,y} p^\dagger_y & \text{if } (x \sim y) \\ -p_x p_y p^\dagger_x p^\dagger_y & \text{if } (x \nsim y) \end{cases} \tag{4.71}$$

$$p^\dagger_x p_x h_y h^\dagger_y = \begin{cases} -p_x p^\dagger_x h_y h^\dagger_y + h_y h^\dagger_y & \text{if } (x \sim y) \\ -p_x p^\dagger_x h_y h^\dagger_y + h_y h^\dagger_y & \text{if } (x \nsim y) \end{cases} \tag{4.72}$$

$$h_x h^\dagger_x p^\dagger_y p_y = \begin{cases} -h_x h^\dagger_x p_y p^\dagger_y + h_x h^\dagger_x & \text{if } (x \sim y) \\ -h_x h^\dagger_x p_y p^\dagger_y + h_x h^\dagger_x & \text{if } (x \nsim y) \end{cases} \tag{4.73}$$

$$h_x h^\dagger_x h_y h^\dagger_y = \begin{cases} -h_x h_y h^\dagger_x h^\dagger_y + h_x \delta_{x,y} h^\dagger_y & \text{if } (x \sim y) \\ -h_x h_y h^\dagger_x h^\dagger_y & \text{if } (x \nsim y). \end{cases} \tag{4.74}$$

Writing down Eq.(4.70) in terms of these components, we get

$$\begin{aligned} 4S^{33}_{--} =& \sum_{x,y(x \sim y)} \left( -p_x p_y p^\dagger_x p^\dagger_y + p_x p^\dagger_x h_y h^\dagger_y + h_x h^\dagger_x p_y p^\dagger_y - h_x h_y h^\dagger_x h^\dagger_y \right) \\ &+ \sum_x \left( p_x p^\dagger_x + h_x h^\dagger_x \right) \\ &- \sum_{x,y(x \nsim y)} \left( -p_x p_y p^\dagger_x p^\dagger_y + p_x p^\dagger_x h_y h^\dagger_y + h_x h^\dagger_x p_y p^\dagger_y - h_x h_y h^\dagger_x h^\dagger_y \right) \end{aligned} \tag{4.75}$$

where the $(x \nsim y)$ part picks up a minus sign due to the antiferromagnetic term in the sublattices. To perform the normal ordering, some additional squared order terms appear, however, these cancel in the antiferromagnetic sum. The functional form of the observable can then be computed by using

the Wicks theorem, differentiating w.r.t the added source terms. Doing so results in the following functional form of the observable,

$$\begin{aligned}
4S^{33}_{--} = &\sum_t \Bigg\{ \sum_{x,y(x\sim y)} \big( M^{-1}_{(y,t)(y,t+1)} M^{-1}_{(x,t)(x,t+1)} - M^{-1}_{(x,t)(y,t+1)} M^{-1}_{(y,t)(x,t+1)} \\
&+ M^{\dagger-1}_{(y,t)(y,t+1)} M^{-1}_{(x,t)(x,t+1)} + M^{-1}_{(y,t)(y,t+1)} M^{\dagger-1}_{(x,t)(x,t+1)} \\
&+ M^{\dagger-1}_{(y,t)(y,t+1)} M^{\dagger-1}_{(x,t)(x,t+1)} - M^{\dagger-1}_{(x,t)(y,t+1)} M^{\dagger-1}_{(y,t)(x,t+1)} \big) \\
&+ \sum_x \big( M^{-1}_{(x,t)(x,t+1)} + M^{\dagger-1}_{(x,t)(x,t+1)} \big) \\
&- \sum_{x,y(x\nsim y)} \big( M^{-1}_{(y,t)(y,t+1)} M^{-1}_{(x,t)(x,t+1)} - M^{-1}_{(x,t)(y,t+1)} M^{-1}_{(y,t)(x,t+1)} \\
&+ M^{\dagger-1}_{(y,t)(y,t+1)} M^{-1}_{(x,t)(x,t+1)} + M^{-1}_{(y,t)(y,t+1)} M^{\dagger-1}_{(x,t)(x,t+1)} \\
&+ M^{\dagger-1}_{(y,t)(y,t+1)} M^{\dagger-1}_{(x,t)(x,t+1)} - M^{\dagger-1}_{(x,t)(y,t+1)} M^{\dagger-1}_{(y,t)(x,t+1)} \big) \Bigg\},
\end{aligned} \tag{4.76}$$

which we can reduce to

$$\begin{aligned}
4S^{33}_{--} = \sum_t \Bigg\{ &\sum_{x,y} \Big( 2\,\mathrm{Re}\left[ (A_y M^{-1}_{(y,t)(y,t+1)})(A_x M^{-1}_{(x,t)(x,t+1)}) \right] + 2(A_y M^{\dagger-1}_{(y,t)(y,t+1)})(A_x M^{-1}_{(x,t)(x,t+1)}) \Big) \\
&+ \sum_x 2\,\mathrm{Re}\left[ M^{-1}_{(x,t)(x,t+1)} \right] - \sum_{x,y(x\sim y)} 2\,\mathrm{Re}[M^{-1}_{(x,t)(y,t+1)} M^{-1}_{(y,t)(x,t+1)}] \\
&+ \sum_{x,y(x\nsim y)} 2\,\mathrm{Re}\left[ M^{-1}_{(x,t)(y,t+1)} M^{-1}_{(y,t)(x,t+1)} \right] \Bigg\}.
\end{aligned} \tag{4.77}$$

### 4.6.1 Expectations

What are our expectations for the two observables, the antiferromagnetic spin $\langle S^3_- \rangle$ and the two-piont function of the antiferromagnetic spin, $\langle S^{33}_{--} \rangle$?
In Ref.[27], a detailed explanation of the different observables of Graphene have been given (in the case of a Hubbard interaction). They also investigate the critical behavior for both the non-interacting ($U \to 0$) and non-hopping ($\kappa \to 0$) limits of the system.
Let us first consider the case where we have no interaction ($V = 0$) and no mass ($m = 0$). The particle/holes number $p_x p^\dagger_x (h_x h^\dagger_x)$, which simply determines the number of particles/holes, will give the total number of unit cells $N = L_m L_n$. Introducing the staggered mass does not influence the global sum over all sites, however, locally pushes the particles and holes in favor of one of the sublattices. If we now look at the antiferromagnetic spin $\langle S^3_- \rangle$, which is described by Eq.(4.63), we can see that in the non-interacting case ($V = 0$), without a staggered mass ($m = 0$), the two sublattices have on average an equal number of particles and holes, such that the expectation value cancels to zero. In the case we added a staggered mass ($m \neq 0$), this average is pushed in favor of one of the sublattices, thus inducing a non-zero value for the sublattice spin difference which increases linearly with the mass ($\langle S^3_- \rangle(m) \propto m$). The staggered mass creates a band gap, as seen in section 1.2. If we now consider the case in which we only have our Coulomb interaction ($V \neq 0,\ \kappa = 0,\ m = 0$), then the system will be frozen in the ground-state of the interacting potential in which each site has a single up- or down- electron per site at half-filling[33]. In terms of particles and holes, this translates to one of the sublattices have both a particle and a hole, and the other sublattice having neither. This state is highly degenerate and the expectation value of the sublattice spin difference will result in zero. The AF spin will, therefore, on average also remain the same, again being pushed in favor of one sublattice when a staggered mass is added. The AF spin will therefore always result in a vanishing contribution at half-filling, given that $m = 0$, independent of the interaction strength. We can explain the vanishing result by looking at magnetization in the classical Ising spin model. In the Ising spin model, the

energy is determined by the spin of nearest-neighbors, Two neighbors with equal spin will contribute as 1, and two with opposite spins as -1. Above some critical point, all the spins align in one of the two possible spins (either up or down), however, the probability of being all up or all down is the same. If we would now compute an expectation value of the magnetization (the sum of all spins) over many configurations, this will give zero. The expectation value of the magnetization in the Ising model will give zero, because on average the state of all up or all down have equal probability of occurring, and thus cancel each other in the average.
Above the critical point, the charge distribution of Graphene will organize onto one of the sublattices, breaking sublattice symmetry. The charge distribution for the strong coupling ground state of Graphene has one sublattice fully occupied and one empty. However, the state is degenerate in the sublattice which is occupied. We thus have that, analogous to the magnetization in the Ising model, the expectation value of many configurations is zero.

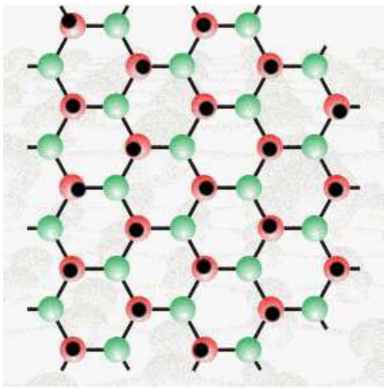

Figure 4.3: The graphene lattice with one of the sublattices being occupied and the other being empty taken from Ref.[33]

The order parameters which then does show a phase transition, is the square of the AF spin, $\langle S^{33}_{--}\rangle$. In the case of the Ising spin model, the order-parameter is the square magnetization $\langle M^2\rangle$, as this will result in 1 for both a system of fully up and fully down spins. The square of the AF spin $\langle S^{33}_{--}\rangle$ would also resolve this averaging problem and is therefore the order-parameter to look at. In the non-interacting ($V = 0$) case without a staggered mass ($m = 0$), the AF spin two point function gives a constant value of 1/2[27]. When a mass is introduced, this is again shifted upwards and will increase quadratically as a function of the mass ($\langle S^{33}_{--}\rangle(m) \propto m^2$). If we introduce interactions, we expect a phase transition to occur above some critical $\alpha_{\text{eff}}$. This phase transition can be described by the interacting potential, introducing a bias in the sublattice as the relative strength of the hopping decreases compared to the interaction, favoring one of the sublattices over the other. Below the critical point, the interaction strength is not enough to induce this bias. The system size will be hugely important in determining this transition. In the case of a Hubbard interaction potential, the limit in which $\kappa = 0$ and $m = 0$ results in $\min(N, (\kappa\beta/\pi)^2)$[27]. In the case of our screened Coulomb potential a similar behavior would be expected, however, no exact solution has been determined. Our expectations are summarized in the table below.

| Observable | $m = 0, V = 0$ | $\kappa = 0, m = 0$ | $V = 0$ | $\kappa = 0$ |
|---|---|---|---|---|
| $\langle S^3_-\rangle$ | 0 | 0 | $\propto m$ | $\propto m$ |
| $\langle S^{33}_{--}\rangle$ | 1/2 | $N$ | $\propto m^2$ | $\propto m^2$ |

# Chapter 5

# Non-interacting Graphene

Before investigating the interacting system of graphene, let us look into a case in which we can analytically compare the implementation. This will be done by looking at non-interacting graphene as discussed in section 1.2. In this case, we expect to be in a conducting phase with no mass-gap, and no sublattice symmetry breaking.

## 5.1 Non-interacting Tight-binding model of Graphene

We will be looking at the system of non-interacting graphene, described by a tight-binding Hamiltonian with an added staggered mass term. To compare the fermionic matrix of graphene and the analytical Hamiltonian implementation, we will compare the correlator $\langle a_{x,\tau} a^{\dagger}_{y,0} \rangle$ of the two methods.
For the analytical problem we will look at a finite size system to purely check if the two methods are comparable. We will again be working with the Hamiltonian of the tight-binding model, Eq.(4.4), with an added mass term Eq.(4.5). In this case we will look at the tight-binding model without spin, and we will do the same for the fermionic Matrix (which is the same for both up and down spin). Since there is a particle-hole symmetry, the resulting fermionic matrix $M$ will be the same as Eq.(4.28), with $\phi = 0$.
To compare the non-interacting model of graphene as discussed in section 1.2, to the path integral formalism, described in the previous sections, we will look at the correlator of the system. To obtain the Green's function for the non-interacting system which obeys

$$(i\partial_t - H)G_{x,t,x't'} = \delta_{x,x'}\delta_{t,t'}, \tag{5.1}$$

we can compute the inverse in k-space as

$$\begin{aligned} G^{-1}(\omega, k) =& i\omega\mathbb{I} + h_k \\ =& \begin{pmatrix} i\omega + m & -\kappa\Delta_k \\ \Delta_k^* & i\omega - m \end{pmatrix}, \end{aligned} \tag{5.2}$$

where we can thus obtain the Green's function by taking the inverse. The $\omega$ is the Matsubara frequencies, which for fermions are $\omega_n = \frac{\pi(2n+1)}{\beta}$. In our problem we have a discretized temporal grid and thus the Matsubara frequencies are also discretized. The time derivative of the Lagrangian is discretized in a forward manner,

$$\partial_\tau f(t) \to \frac{1}{\delta}(\delta_{\tau+\delta,t} - \delta_{\tau,t})f(t). \tag{5.3}$$

If we perform the temporal Fourier transform

$$f(\omega) = \frac{1}{\beta}\sum_{t=0}^{Nt-1} f(t)e^{-i\omega t} \tag{5.4}$$

which is obtained from

$$\delta_{t_i,t_j} = \frac{1}{\beta}\sum_{n=-Nt/2}^{Nt/2-1} e^{i\omega_n(t_i-t_j)}, \tag{5.5}$$

on our discretized derivative we obtain

$$\begin{aligned}\frac{1}{\delta}(\delta_{\tau+\delta,t}-\delta_{\tau,t})f(t) =& \frac{1}{\beta\delta}\sum_n \left(e^{i\omega_n(\tau+\delta-t)} - e^{i\omega_n(\tau-t)}\right) f(t)\\ =& \frac{1}{\beta\delta}\sum_n e^{i\omega_n(\tau-t)}e^{i\omega_n\delta/2}\left(e^{i\omega_n\delta/2} - e^{-i\omega_n\delta/2}\right) f(t)\\ =& \frac{2i}{\beta\delta}\sum_n e^{i\omega_n(\tau-t)}e^{i\omega_n\delta/2}\sin\big(\omega_n\delta/2\big) f(t),\end{aligned} \tag{5.6}$$

such that the forward derivative can be replaced by

$$\partial_\tau f(t) \to \frac{1}{\beta}\sum_n e^{i\omega(\tau-t)}\frac{2i}{\delta}e^{i\omega\delta/2}\sin\big(\omega_n\delta/2\big) f(t). \tag{5.7}$$

By adding this to our description of the inverse Green's function, we obtain with the use of a forward discretized time derivative it is given by

$$G^{-1}(\omega,k) = \begin{pmatrix} \frac{2i}{\delta}e^{i\omega\delta/2}\sin\big(\omega_n\delta/2\big) + m & -\kappa\Delta_k \\ -\kappa\Delta_k^* & \frac{2i}{\delta}e^{i\omega\delta/2}\sin\big(\omega_n\delta/2\big) - m \end{pmatrix}, \tag{5.8}$$

allowing us to compare it to the fermionic matrix of our lattice field theory.

### 5.1.1 Fermionic matrix Green's function

Now, to obtain the Green's function from our fermionic matrix, we have the partition function for the non-interacting system of a single spin

$$\mathrm{Tr}\Big(e^{-\beta H}\Big) = \int\prod_{t=0}^{N_t-1}\left[\prod_x d\psi^*_{x,t}d\psi_{x,t}\right] e^{-\sum_{x,y}\sum t,t'(\psi^*_{x,t}M_{(x,t)(y,t')}\psi_{y,t'})}, \tag{5.9}$$

with

$$M_{(x,t)(y,t')} = \delta_{x,y}(\delta_{t,t'}-\delta_{t-1,t'}) - \kappa\frac{\beta}{N_t}\sum_{\vec{n}}\delta_{y,x+\vec{n}}\delta_{t-1,t'} + m_x\frac{\beta}{N_t}\delta_{x,y}\delta_{t-1,t'}. \tag{5.10}$$

The Green's function of the system can then simply be obtained by taking the correlator

$$\langle a_{x,\tau}a^\dagger_{y,0}\rangle = M^{-1}_{(x,\tau)(y,0)} = -G(x,y,\tau), \tag{5.11}$$

as shown in Eq.(4.62). We wish to compare the Green's function obtained from the analytical method described above, and from the path-integral formalism with each other, for this we will Fourier transform both the analytical to real space and the fermionic matrix to Fourier space. For the analytical method, we also need to perform the sum over Matsubara frequencies.

### 5.1.2 Fourier transforms

To compare the analytical Green's function to the fermionic matrix Eq.(5.10), we will Fourier transform the different results using the following definitions of the Fourier transform;

$$f_k = \tfrac{1}{\sqrt{N}}\textstyle\sum_{x\in\{x\}} f_x e^{-ikx}, \qquad f_x = \tfrac{1}{\sqrt{N}}\sum_{k\in\{k\}} f_x e^{ikx}, \tag{5.12}$$

$$g_{w_n} = \tfrac{1}{\sqrt{\beta}}\textstyle\sum_{t=0}^{Nt-1} f_t e^{-i\omega_n t}, \qquad g_t = \tfrac{1}{\sqrt{\beta}}\sum_{n=-Nt/2}^{Nt/2-1} g_{w_n} e^{i\omega_n t}, \tag{5.13}$$

where $\{x\}$ are all sites on the sublattice and $\{k\}$ the momentum points inside the Brillouin zone. We can directly compute the real space correlator from the inverse of our fermionic matrix and compare this with the analytical Green's function by performing a Fourier transform to real space and time. We also look at the temporal k-space correlator:

$$G_{k,t,k',t'} = \frac{1}{\beta} \sum_{n,n'=-Nt/2}^{Nt/2-1} e^{-i\omega_n t} G(\omega, k) \delta_{\omega,\omega'} \delta_{k,k'} e^{i\omega'_n t'} \tag{5.14}$$

from which we can compute the real space correlator

$$G_{x,t,y,t'} = \frac{1}{N} \sum_{k\in\{k\}} e^{ikx} G_{k,t,k',t'} e^{-ik'y}. \tag{5.15}$$

The fermionic matrix in k-space is computed as

$$M^{-1}_{k,k',t,t'} = \frac{1}{N} \sum_{x\in\{x\}} e^{-ikx} M^{-1}_{(x,t)(y,t')} e^{ik'y}. \tag{5.16}$$

## 5.2 Green's function

Let us now compare the two methods, first by looking at the spatial correlator, and second by looking in k-space, both as a function of time. We will look at the spatial correlator $G(x,t,x',t')$ on the four different sublattice combinations $(AA, AB, BA, BB)$ within one unit cell. The correlators are shown in Fig.5.1, in which we see that the discrete analytical and fermionic matrix match perfectly. The correlators shown were those with a lattice grid of $L_m = 12$, $L_n = 12$, with a staggered mass of $m = 0.5$eV. For the discrete and fermionic matrix a temporal discretization of $N_t = 28$ was used and for the continuum limit $N_t = 512$. We see that the $AB$ and $BA$ are identical and that the $AA$ and $BB$ correlator are shifted due to the staggered mass. For the Green's function in k-space (see figure 5.2) we have taken a point at the center of the Brillouin zone, $k = \frac{\pi}{3a}(\sqrt{3}, 1)^T$. Here we see the same behavior as the spatial correlator.

## 5.3 Sublattice spin difference

Now let us look at the sublattice spin difference $S^3_-$ in the non-interacting case. To do so, we will work with both spin up and spin down particles, which in the particle hole basis without interactions lead to two identical fermionic matrices given by Eq.(5.10). We can still use the functional form for $\langle S^3_- \rangle$ as derived in section 4.6, where we now do not need to perform an integral over the $\phi$ field. For the analytical representation, we can compute the sublattice spin difference as

$$\langle S^3_- \rangle = 2\Big( \sum_{x\in\{A\}} \langle p^\dagger_x p_x \rangle - \sum_{x\in\{B\}} \langle p^\dagger_x p_x \rangle \Big), \tag{5.17}$$

due to the particle-hole symmetry. The correlater can be rewritten in terms of our Green's function correlater,

$$\langle a^\dagger_x a_x \rangle = -\langle a_x a^\dagger_x \rangle + 1, \tag{5.18}$$

resulting in

$$\begin{aligned} \langle S^3_- \rangle &= -2\Big( \sum_{x\in\{A\}} \langle a_x a^\dagger_x \rangle - \sum_{x\in\{B\}} \langle a_x a^\dagger_x \rangle \Big) \\ &= -2\Big( \sum_{x\in\{A\},\tau} G(x, \tau+1, x, \tau) - \sum_{x\in\{B\},\tau} G(x, \tau+1, x, \tau) \Big) \\ &= -2(G_{AA} - G_{BB}). \end{aligned} \tag{5.19}$$

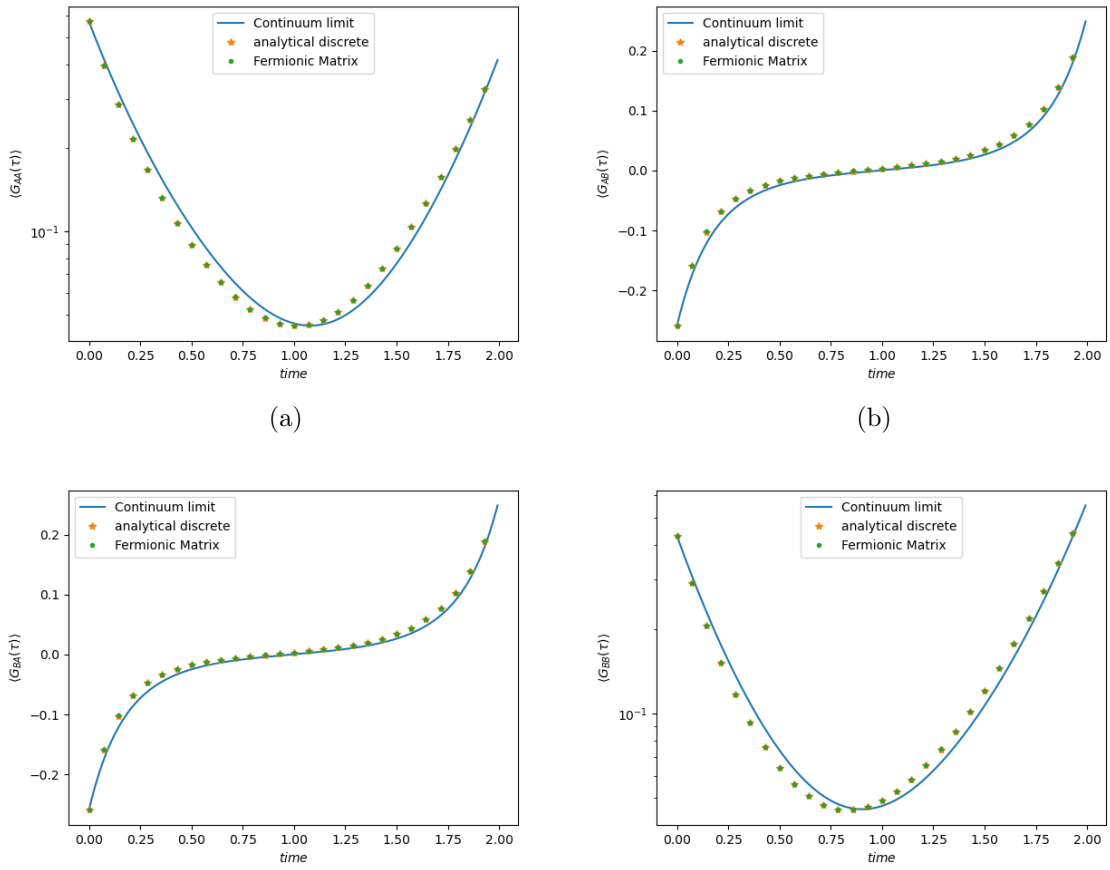


Figure 5.1: Graphene correlator in real space, comparing the fermionic matrix and analytical correlator. (a) is $G_{AA}$, (b): $G_{AB}$, (c):$G_{BA}$ and (d): $G_{BB}$

In fig. 5.3 we see that the two value match. The dimensions of the system used are $L_m = 6,\ L_n = 6,\ N_t = 16$. The analytical continuum limit result is also shown ($\delta t \to 0$, by using $N_t = 512$). Here we can see that the discrete analytical and fermionic matrix match as expected, however, they deviate from the continuum. Increasing the number of time-steps brings the discrete solutions closer to the continuum, at some point giving matching results.

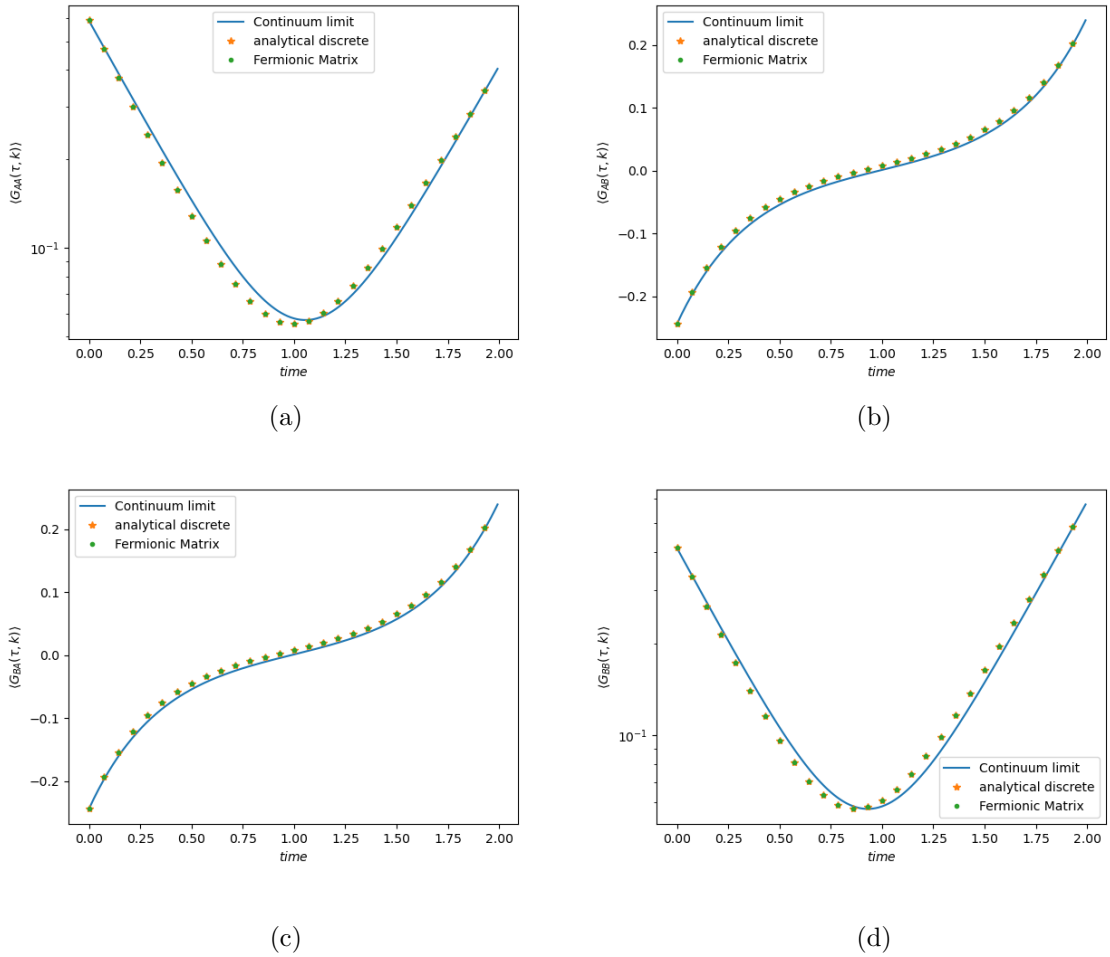


Figure 5.2: Graphene correlator in k-space at $k = \frac{\pi}{3a}(\sqrt{3}, 1)^T$, comparing the fermionic matrix and analytical correlator. (a) $G_{AA}$, (b) $G_{AB}$, (c) $G_{BA}$ and (d) $G_{BB}$

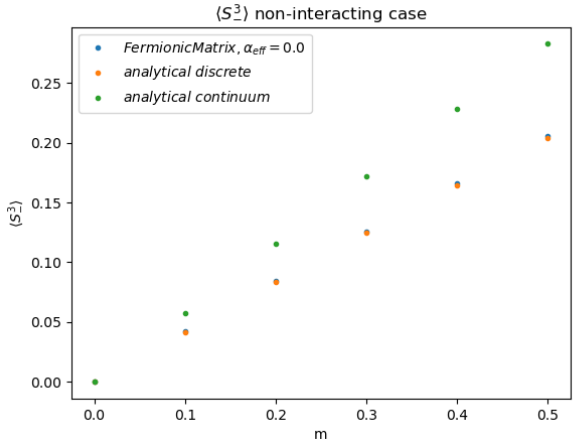


Figure 5.3: The analytical and fermionic matrix sublattice spin difference $\langle S^3_- \rangle$ for different values of the staggered mass $m$.

# Chapter 6

# Results

Now that we have investigated the lattice field theory approach, and the tight-binding model by which we can describe graphene, let us look at the order-parameters which quantify the sublattice symmetry breaking; $\langle S^3_- \rangle$ and $\langle S^{33}_{--} \rangle$.

To perform our calculations, an HMC algorithm, following the method described in the previous section, has been implemented in the programming language *Julia*[34]. The implementation can be found in the git repository in Ref.[35]. For each measurement, a HMC calculation is performed computing $N_{samples}$ different configurations $\phi_i \in \{\phi\}$. The compact linked fermionic matrix Eq.(4.28) is used for the calculations. Each configuration is obtained by performing a Hamiltonian dynamics path of length $L$ in steps of size $\epsilon$. The path is computed using a Sexton-Weingarten multiscale integrator with two scales: for the Hubbard force Eq.(4.44) a scale of $\epsilon$ and for the fermion force Eq.(4.50) a scale of $\epsilon/m_{sw}$. The integer $m_{sw}$ was kept fixed at $m_{sw} = 5$, the trajectory length was kept fixed at $L = 10$ for all calculations and $\epsilon$ was varied dependent on the acceptance rate. The inverse temperature $\beta$ was set fixed at $\beta = 2.0\text{eV}^{-1}$ for all measurements, similar to Ref.[5]. Since the $\phi$ field is a non-compact variable, the field can move arbitrarily far away from thermal equilibrium. Although the HS field $\phi$ enters as a compact link in the fermionic matrix (e.i. $e^{-i\phi}$), it does not in the action. The choice of a proper starting position is therefore not trivial. The acceptance rate is highly dependent on its distance from equilibrium, being greatly reduced when far away from equilibrium. Each calculation performs $N_{\text{burn in}} = 100$ burn in samples, in which the step size of the Hamiltonian dynamics is reduced to $\epsilon_{\text{burn in}} = \epsilon/5$ to decrease the energy deviation and no Metropolis check is performed. This burn-in is performed in the aim to have faster convergence to a region in which a higher acceptance rate is found (closer to equilibrium). After the burn-in samples, $N_{\text{offset}}$ thermalization samples are removed from the configurations to reduce the dependency on the initialization further. Performing the burn-in and removing the offset ensures that the samples to which the expectation value is computed are those from the desired target distribution $p(\phi)$.
For each choice of $\alpha_{\text{eff}}$, we perform simulations with staggered mass $m = 0.5, 0.4, 0.3, 0.2, 0.1\text{eV}$ in this order. Calculations with the largest mass ($m = 0.5\text{eV}$) are much cheaper to perform in terms of computation time, since the inversion is faster. The final state $\phi$ of the $m = 0.5\text{eV}$ calculation is then used as the initial state of the next mass calculation ($m = 0.4\text{eV}$), after which again burn-in and thermalization steps are performed and removed. This process of using the final configuration as the start of the next is used for all masses. Proceeding from the previous mass greatly improves the thermalization, reducing the number of steps needed to come in a region of high acceptance.

To produce results without a staggered mass, an extrapolation is performed taking the result to the $m \to 0$ limit. The result in the $m \to 0$ limit is obtained by doing a least square fit to a 2nd order polynomial,

$$\langle O \rangle(m) = c_1 m^2 + c_2 m + c_3. \tag{6.1}$$

The extrapolation is done in the same manner for both the sublattice spin difference $\langle S^3_- \rangle$ and its square order parameter $\langle S^{33}_{--} \rangle$. In section 6.3, we will briefly discuss the extrapolations.

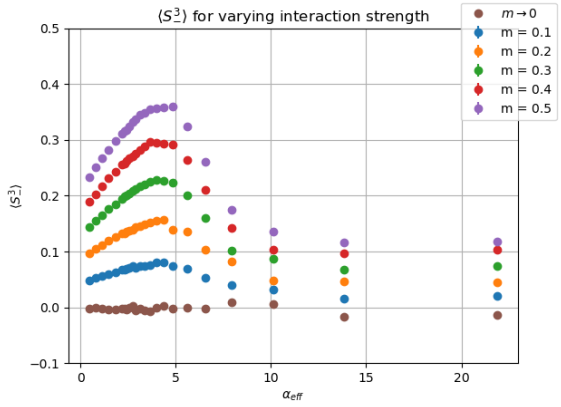


(a) Measurements of the sublattice spin difference $S^3_-$ at varying $\alpha_{\text{eff}}$ for the different staggered mass values.

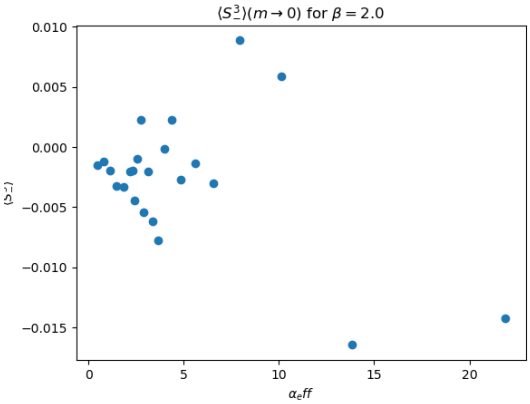


(b) Results of the AF spin $\langle S^3_- \rangle$ after performing the mass extrapolation $m \to 0$.

Figure 6.1: The measurement results for the sublattice spin difference $\langle S^3_- \rangle$ for a system of $L_m = 4$, $L_n = 4$ with $N_t = 16$.

## 6.1 Antiferromagnetic spin $\langle S^3_- \rangle$

We will first investigate the sublattice spin difference $\langle S^3_- \rangle$, using the compact linked fermionic matrix Eq.(4.28). The calculations have been performed with $N_t = 16$ discrete euclidean time steps, on a hexagonal grid of $L_m = 4$, $L_n = 4$, using periodic boundary conditions. The aim of the calculations is to reproduce the results found by Ref.[5], in which a critical point at $\alpha_c \approx 3.14$ was found, however, in their calculations a system of size $L_m = 18,\ L_n = 18,\ N_t = 20$ was used.

Measurements of the $S^3_-$ observable have been performed on a range of $\alpha_{\text{eff}}$, the results for the measurements for each of the five different staggered masses are shown in Fig.6.1a, as well as the extrapolation result to the $m \to 0$ limit. The simulation results are computed by sampling $N_{\text{samples}} = 10k$ configurations $\phi_i$, of which the first $N_{\text{offset}} = 3k$ are removed.
The simulations have been performed with two different values of the step size $\epsilon$ in the Hamiltonian dynamics. The region $\alpha_{\text{eff}} \in [0.25, 5.0]$ was computed with $\epsilon = 0.5$ and $\alpha_{\text{eff}} \in [5.0, 22.5]$ with $\epsilon = 0.25$. The change of the step size was to improve the acceptance rate in the calculations. With an increase in the interaction strength, the acceptance rate greatly decreased due to an increase in the error for each integration step in the Hamiltonian dynamics path. To overcome this the step-size is decreased, however, still a considerable amount of points was rejected.
The results show a clear behavior dependent on the mass. As expected the staggered mass pushes the spin configurations to a certain antiferromagnetic direction. When the staggered mass is increased this therefore results in a higher value of the sublattice spin difference. This can clearly be seen, showing a linear behavior with an increase in the mass as expected for all values of $\alpha_{\text{eff}}$. We can see a clear dependency on the interaction strength for the simulations with an added mass. The extrapolations, however, remain zero for all values of $\alpha_{\text{eff}}$. As discussed in section 4.6.1, analogous to the idea of magnetization in an Ising model the average of configurations will cancel, resulting in an expectation value of zero. If we Look at the results with an added mass, we see a steady increase and peak after which the order parameter decreases again.
This behavior can be described in terms of the following; In the first region ($\alpha_{\text{eff}} < 3$), we are near the non-interacting limit ($V \approx 0$), where we have that $V \ll \kappa$ and $V \ll m$. As V increases, so does the AF spin. As the system moves away from the non-interacting case, we have that $V \approx \kappa$ $V \approx m$ increasing the order parameter to the highest value. Now as we continue increasing the strength, we go to a region which can be approximated to be purely interacting theory ($V \gg \kappa$ and $V \gg m$). We still see the linear separation caused by the mass term in the order parameter, however have an overall scale decrease. The system effectively goes to a case in which we can approximate that $\kappa \sim 0$.

Removing the hopping and only having a dependency on the staggered mass and the potential.

## 6.2 Thermodynamic limit

To be able to give accurate results, both a thermodynamic limit and continuum limit should be performed. To see if a phase transition occurs in the squared AF-spin order parameter, we will perform one of these limits, the thermodynamic limit. The thermodynamic limit will be applied by computing all measurements at three different volumes ($N = L_m L_n = 2^2,\ 4^2,\ 6^2$) and extrapolating to the $1/N \to 0$ limit ($N \to \infty$). The temporal discretization was kept fixed at $N_t = 16$. The thermodynamic limit extrapolation to $N \to \infty$ was performed using a 2nd order polynomial. After performing the thermodynamic limit, the mass limit $m \to 0$ is performed. The order in which the limits are performed is important. In a small system, the mass term has a greater influence in the energy relative to the coulomb and tight-binding term. If we were to perform the mass limit first then this influence would be found in the result. If we first perform the thermodynamic limit, given that the system sizes chosen to perform the extrapolation are large enough, then the influence on the overall energy of the system to the mass term is reduced, optimally reaching a good thermodynamic limit. This however only works in the case that the system sizes chosen are large enough.

The measurements will be performed with $N_{\text{samples}} = 5K$ of which the first $N_{\text{offset}} = 1.5K$ samples are removed. For the simulations at $N = 2^2$ and $4^2$ the step size $\epsilon = 0.5$ with Sexton-Weingarten factor $m_{sw} = 5$ is used. For the simulations at $N = 6^2$ the same step size is used however to increase the acceptance rate the SW factor was increased to $m_{sw} = 8$.

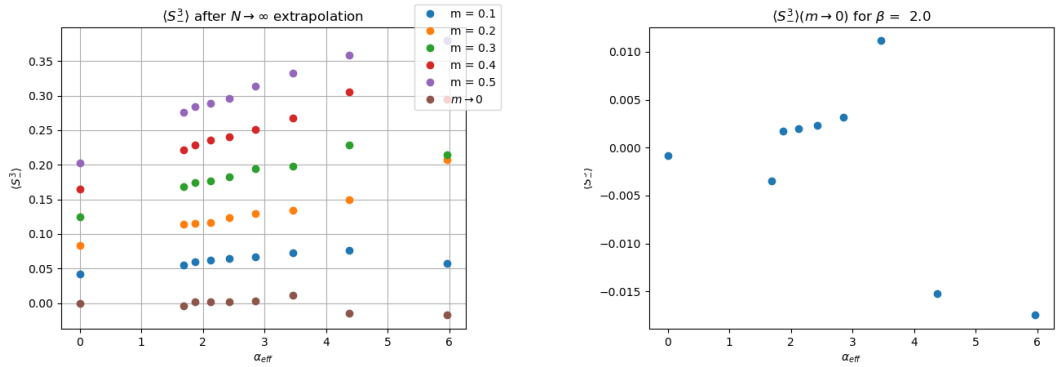


(a) Calculation results for $\langle S^3_- \rangle$ of the various masses.

(b) Mass extrapolation result of $\langle S^3_- \rangle$ after performing the thermodynamic limit.

Figure 6.2: Calculation results of the sublattice spin difference $\langle S^3_- \rangle$ after performing the thermodynamic limit using systems of size $N = 2^2, 4^2, 6^2$.

Before going to the square AF spin order parameter, let us investigate if the AF spin is influenced by performing the thermodynamic limit. In Fig.6.2, the results after the thermodynamic limit extrapolation are shown for each mass as well as the final mass limit extrapolation results. Here we can see that the combination of the two limits stil leads to a final result of zero for all the $\alpha_{\text{eff}}$ measured. Looking at the final extrapolation result in Fig,6.2b we see that all results are roughly zero. We do see a change in the behavior for the larger $\alpha_{\text{eff}} > 3.2$ results. This behavior is however mostly due to an increase in the correlation between points of the HMC samples. The number of samples computed is therefore not enough to properly capture the full scope of the integral and more points should be sampled.

Let us now look at the square AF spin $\langle S^{33}_{--} \rangle$, performing the thermodynamic $N \to \infty$ followed by mass $m \to 0$ limit extrapolations. In Fig.6.3 the results are shown. We can see that the extrapolation

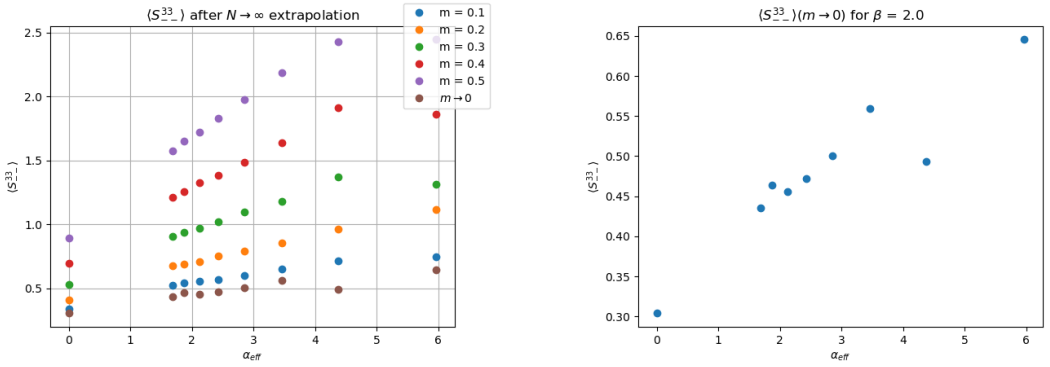


(a) Calculation results for $\langle S^{33}_{--} \rangle$ of the various masses.

(b) Mass extrapolation result of $\langle S^{33}_{--} \rangle$ after performing the thermodynamic limit.

Figure 6.3: Calculation results of the sublattice spin difference $\langle S^3_- \rangle$ after performing the thermodynamic limit using systems of size $N = 2^2, 4^2, 6^2$.

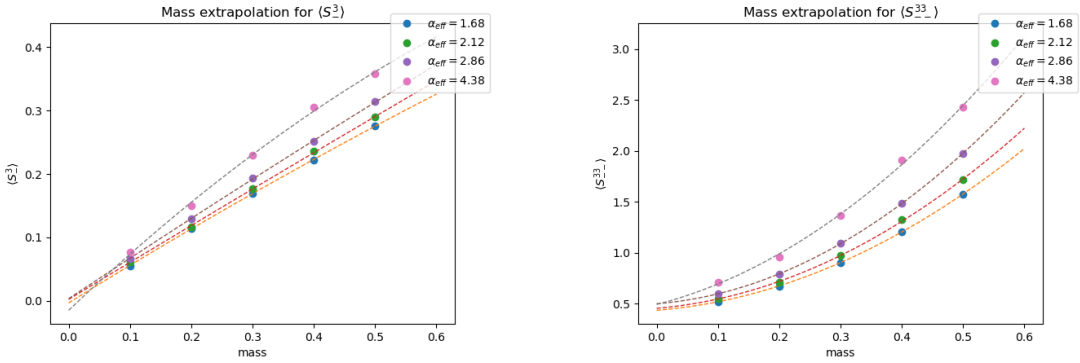


(a) Mass extrapolation fit for $\langle S^3_- \rangle$

(b) Mass extrapolation fit for $\langle S^{33}_{--} \rangle$

Figure 6.4: A few of the mass extrapolation fits for both $\langle S^{33}_{--} \rangle$ and $\langle S^{33}_{--} \rangle$

results are roughly around $\langle S^{33}_{--} \rangle \approx 1/2$, which is the predicted non-interacting result, however, no clear phase transition can be seen in the results. The system sizes used for the thermodynamic limit are too small to capture the needed information. Additionally, the temporal discretization is to course for accurate results near the continuum limit. These finite size issues make that no conclusive predictions can be made on the presence of a phase-transition based on our measurements.

## 6.3 Mass extrapolation

During the measurements the mass limit is performed taking the staggered mass to zero. In section 4.6.1, we discussed the expectations of the increase of both the $\langle S^3_- \rangle$ and $\langle S^{33}_{--} \rangle$ with an increase in mass. We expected that the AF spin order parameter would behave linearly with an increase in the mass $\langle S^3_- \rangle(m) \propto m$, and the square AF spin order parameter $\langle S^{33}_{--} \rangle$ would behave quadratically, $\langle S^{33}_{--} \rangle \propto m^2$. In Fig.6.4, a few of the mass extrapolation are shown with their predicted polynomial fit curve based on Eq.(6.1) for both order parameters. The measurements shown here are the thermodynamic limit extrapolation results as discussed in the previous section. In this figure, we can see that indeed the AF spin behaves linearly and the square AF spin quadratically. We can also see that this behavior slightly changes with larger effective fine-structure constant $\alpha_{\text{eff}}$, this can mostly be explained in a decrease in the acceptance rate of the HMC method at larger coupling, resulting in a lower accuracy in the measurements.

# Chapter 7

# Conclusion

The aim of this work was to investigate the phase-transition in which Graphene goes from a conductor (semimetal) to an insulator, dependent on the *effective* fine-structure constant $\alpha_{\text{eff}}$. At this phase-transition, sublattice symmetry is broken. The order-parameter used to quantify the transition is therefore the sublattice spin difference. To investigate this phase transition, we resorted to the numerical method of lattice field theory. To do so, the theory of Graphene is written in path-integral formalism with discretized euclidean time. To be able to compute the observables, world-lines (or paths) in the path integral are sampled. The weight of these world-lines is dependent on the discrete action of the theory. This weight can, however, be negative which does not allow for the use of the numerical integration method of Monte Carlo Integration. This problem is known as the sign problem. For lattice field theory, Hybrid Monte Carlo is used to approximate the path-integrals. In this method world-line samples are obtained by performing a molecular dynamics path between samples and accepting them based on the Metropolis-Hastings acceptance, such that they follow the distribution $e^{-S}$. The theory of graphene contains a Tight-binding term and Coulomb interaction. It can be written in a basis which is free of the sign problem by making use of the fact that the theory has a particle-hole symmetry and that the hexagonal lattice is bipartite. This was done by writing the Graphene Hamiltonian in the terms of the particle-hole basis and performing a sign flip on the hole operator on one of the two sublattices. Besides these transformations a Hubbard-Stratonovich transformation is performed which removes the 4th order interactions terms and replaces them with second order terms coupled to an HS field, thus introducing a new degree of freedom the HS field. Additionally, a mass term is added, this term is added to remove zero-modes in the Fermionic matrices of the theory, which otherwise would give numerical issues when the inverse was computed. This mass term is extrapolated to zero to obtain the desired measurements. With these transformations performed the theory of graphene is written in a form suitable for Hybrid Monte Carlo where world lines of the HS fields are sampled.

An implementation of a lattice field theory of graphene was made in `Julia` and can be found in [https://github.com/Rik-Breebaart/GrapheneHMC.git]. With this implementation, measurements have been performed looking at the sublattice spin difference $\langle S^3_- \rangle$, aiming to see a phase-transition dependent on strength of the Coulomb interactions through sublattice symmetry breaking.

In the results, however, no clear phase transition was found. Measurements where performed both on $\langle S^3_- \rangle$ and $\langle S^{33}_{--} \rangle$, the square operator of the sublattice spin. Most measurements where performed on the sublattice spin difference $\langle S^3_- \rangle$ at a fixed system size of $N = 4^2$ with $N_t = 16$ time slices. For the sublattice spin difference no phase transition was found as the theory on average will have the same number of particles and holes on each sublattice independent of the coupling. When performing a thermodynamic limit, taking three different system sizes and extrapolating to $N \to \infty$, no phase-transition was found in both $\langle S^3_- \rangle$ and $\langle S^{33}_{--} \rangle$. No clear conclusion can be made on the presence of a phase transition based on these results. This can mostly be related to finite size. The size of the systems simulated was small, the largest size investigated to perform the thermodynamic extrapolation was $N = 6^2$ and the number of discrete time steps was always $N_t = 16$.

# Chapter 8

# Discussion

There are many factors which contribute to the final results which has been obtained. Both the HMC and LFT components influence the simulation results. In the optimal situation a much larger number of samples would be computed, which have been calculated with smaller step-sizes in the Hamiltonian dynamics path. The system size taken would have been of an order larger, leading to results closer reflecting the infinite volume (thermodynamic limit). The discretization of time would also have been increased, and a continuum limit extrapolation should be performed.
In this discussion chapter, different components which influence the results are briefly discussed.

**Finite size**

The results show no clear phase transition, however, they do show the non-interacting behavior expected as discussed in section 4.6.1. One of the reasons why no phase transition is found for our measurements is the size of the system. The size of the system determines possible discretized energy states available in the dispersion. If the system size is too small, not enough points will be found within the region around the Dirac point, in which the gap is found. To see a phase transition, sample points within the mass gap are needed. If the system size is too small, the points may fall outside the gap, and will thus not capture the phase transition behavior. An increase of system size is needed to capture the full spectrum. The possible number of states in the mass gap is too small to fully consider the region of possible configurations. A possible solution to this problem is reducing the mass gap induced by the added mass term, however, this greatly increases the computation time caused by difficulties in the inversion. To resolve the finite size issue, the thermodynamic limit extrapolation was performed, however, the systems size to perform the extrapolation may have been too small to properly capture the thermodynamic limit behavior.

**Measurement error**

In appendix C, the calculation results of the sublattice spin difference at the different mass values are shown seperatly. In Fig.C.1, the error of the calculations can be seen, which is based on the Monte Carlo error Eq.(2.10). The MC error of the calculations is also included in Fig.6.1, however, is to small relative to the $y$-axis. This error only keeps into account the accuracy of the integral approximation based on the MC method, however, does not take into account the finite size error introduced by the discretization in the path-integral formalism. In Eq.(3.10), the error introduced by the taylor expansion of the exponent at finite $\delta t$ should be taken into account. This error is highly relevant for our results as we only use $N_t = 16$ steps. With our choice of $\beta = 2.0$ and $N_t = 16$ time discretization steps we have that $\delta t = 1/8$. The error of order $\mathcal{O}(\delta t)$ caused by the discretization is therefore highly important.

For the MC to perform accurate calculations and give an accurate prediction of the error, the samples need to be uncorrelated. However, in our work, no thorough investigation has been performed into the autocorrelation of the sampled configurations. For accurate predictions, a thorough investigation in the autocorrelation of the generated samples is needed.

### Computational cost

Unfortunately, the calculation are computationally bound by the computation of inverses of the fermionic matrix. The inverse needs to be computed once at each Hamiltonian dynamics integration step. The inversion is performed using the conjugate gradient function from the `Julia` package `IterativeSolvers`[36]. The computation time is highly dependent on the matrix size, thus increasing the discretization or system size greatly increases the time to obtain each sample. Due to time constraints, only a relatively small system size and temporal discretization is used.

The simulations have been performed on the `TP-Gemini` cluster of Utrecht University, using 6 cores for each measurement at a certain $\alpha_{\text{eff}}$ and computing all measurements of the different masses consecutively. The 6 cores where utilized in parallel for the inversion of the fermionic matrix. The measurements at different $\alpha_{\text{eff}}$ where run simultaneously, using a maximum of 64 cores. The computation time of the simulations is mostly determined by the inversion. The added staggered mass improves the inversion speed, but as the mass decreases the computation time increases. In Ref.[37], a conjugate gradient solver with Hasenbusch preconditioner is used, allowing to work at zero staggered mass. To illustrate the computation time dependent on the system size for a single sample, a $2 \times 2$ lattice with $N_t = 16$ takes $\sim 0.2$s, a $4 \times 4$ lattice with $N_t = 16$ takes $\sim 4.0$s and a $6 \times 6$ lattice with $N_t = 16$ takes $\sim 50.0$s. We thus have that each measurement at a lattice of $4 \times 4$ takes roughly 11 hours for a given $\alpha_{\text{eff}}$ and $m$. To perform the $m \to 0$ extrapolation we then perform five of such calculations at different masses, requiring roughly 2.3 days per $\alpha_{\text{eff}}$. If we were to look at a lattice of $6 \times 6$ for the same number of points this would take about 29 days per $\alpha_{\text{eff}}$. Due to these constraints the measurements performed have been of lower accuracy then would be desired. By improving the computational speed this would allow for larger system sizes (getting closer to the thermodynamic limit), more samples $N_{samples}$ (leading to a more accurate expectation value) and better ability to perform both the thermodynamic and continuum limit.

For each value of $\alpha_{\text{eff}}$ five HMC simulations have to be performed, each at a different staggered mass values. To improve the speed, the conjugate gradient method using Hasenbusch Precondition could be used, removing the need for a mass extrapolation. Implementing the algorithm to work on GPUs would also greatly improve the computational time, since GPUs are much faster at matrix multiplications then CPUs, therefore being far more efficient in performing the inversion. A larger server utilizing more resources and better parallelization would also further improve the computational speed of the measurements.

### hyperparameter choice

A common issue that occurred in the HMC measurements at larger $\alpha_{\text{eff}}$ is that the system might get stuck in some state which the HMC can not move away from. This issue is not caused by an ergodicity problem, in which the HMC algorithm is unable to move passed certain boundaries. The ergodicity problem has been thoroughly discussed in Ref.[7], which also states that the linear representation of the fermionic matrix, which has been used in our implementation does not have such an ergodicity problem. The HMC method gets stuck in a certain state configuration because for some configurations the Hamiltonian dynamics path does not properly conserve energy, leading to a path which is always rejected. This leads to a system which remains in the same state for the remainder of the simulation and occurs mostly at large coupling ($\alpha_{\text{eff}} > 5$). To overcome this problem, the hyperparameters $\epsilon$, $m_{sw}$ and $L$ should be changed accordingly. The choice of hyperparameters for the HMC algorithm is a common problem in such simulations and to find the right parameters which are both computationally efficient and give a good acceptance is difficult. The No-U-turn sampler (NUTS) method[38] is a method which resolves this problem by automatically selecting an appropriate value for $L$. To have better measurement results, the NUTS method may be implemented, removing the dependency of the sampling on the hyperparameters of the path.

### Influence of parameter choice

The LFT algorithm depends on a lot of different parameters and hyperparameters, each influencing the result in some way. Parameters which have influence on the result both in computational cost and accuracy are;

- The discretization step size $N_t$
- The system size $N = L_m L_n$
- The Hamiltonian dynamics integrator step-size $\epsilon$
- The Hamiltonian dynamics path length $L$
- Sexton-weingarten integration step multiplier $m_{sw}$
- Number of burn in steps $N_{\text{burn in}}$ (steps which do not use the metropolis check)
- Number of offset steps $N_{\text{offset}}$
- Total number of configurations $N_{\text{conf}}$

### Implementation

The computational efficiency in which the method is implemented also greatly influence the computation time. A lot of computational improves can still be made in the implementation to further improve the efficiency.

# Acknowledgements

I would like to sincerely thank Lars Fritz for his time, help and guidance during my thesis. He has been of great help discussing my results and placing them into perspective, because sometimes a bad results is also a good result. To Timo Lähde and Evan Berkowitz, for their invaluable discussion on HMC calculations and my results. To everyone at the group of Lars and Dirk for their presentations and nice meetings, I always felt part of the group. To my parents, for being there for me as a listening ear. To Emiel for reading through my work and the great feedback he provided. To Rick and Micheal on talking about work-live balance and sometimes taking a step back to reevaluate. Finally, to all others which have been their for me throughout this journey.

# Bibliography


[1] K. S. Novoselov, A. K. Geim, S. V. Morozov, D. Jiang, Y. Zhang, S. V. Dubonos, I. V. Grigorieva, and A. A. Firsov, "Electric field effect in atomically thin carbon films," *Science*, vol. 306, no. 5696, pp. 666–669, 2004. [Online]. Available: https://www.science.org/doi/abs/10.1126/science.1102896

[2] A. H. C. Neto, F. Guinea, N. M. Peres, K. S. Novoselov, and A. K. Geim, "The electronic properties of graphene," *Reviews of Modern Physics*, vol. 81, pp. 109–162, 1 2009.

[3] J. Ostmeyer, "Stochastic and tensor network simulations of the hubbard model," 10 2022. [Online]. Available: http://arxiv.org/abs/2210.06874

[4] N. M. Peres, "Colloquium: The transport properties of graphene: An introduction," *Reviews of Modern Physics*, vol. 82, pp. 2673–2700, 9 2010.

[5] D. Smith and L. V. Smekal, "Monte carlo simulation of the tight-binding model of graphene with partially screened coulomb interactions," *Physical Review B - Condensed Matter and Materials Physics*, vol. 89, 5 2014.

[6] P. Buividovich, D. Smith, M. Ulybyshev, and L. von Smekal, "Numerical evidence of conformal phase transition in graphene with long-range interactions," 12 2018. [Online]. Available: http://arxiv.org/abs/1812.06435http://dx.doi.org/10.1103/PhysRevB.99.205434

[7] J.-L. Wynen, E. Berkowitz, C. Körber, T. A. Lähde, and T. Luu, "Avoiding ergodicity problems in lattice discretizations of the hubbard model," 12 2018. [Online]. Available: http://arxiv.org/abs/1812.09268http://dx.doi.org/10.1103/PhysRevB.100.075141

[8] R. Brower, C. Rebbi, and D. Schaich, "Hybrid monte carlo simulation on the graphene hexagonal lattice," 4 2012. [Online]. Available: http://arxiv.org/abs/1204.5424

[9] D. C. Elias, R. V. Gorbachev, A. S. Mayorov, S. V. Morozov, A. A. Zhukov, P. Blake, L. A. Ponomarenko, I. V. Grigorieva, K. S. Novoselov, F. Guinea, and A. K. Geim, "Dirac cones reshaped by interaction effects in suspended graphene," *Nature Physics*, vol. 7, no. 9, pp. 701–704, jul 2011. [Online]. Available: https://doi.org/10.1038%2Fnphys2049

[10] C. Popovici, C. S. Fischer, and L. von Smekal, "Fermi velocity renormalization and dynamical gap generation in graphene," 8 2013. [Online]. Available: http://arxiv.org/abs/1308.6199http://dx.doi.org/10.1103/PhysRevB.88.205429

[11] M. V. Ulybyshev, P. V. Buividovich, M. I. Katsnelson, and M. I. Polikarpov, "Monte carlo study of the semimetal-insulator phase transition in monolayer graphene with a realistic interelectron interaction potential," *Physical Review Letters*, vol. 111, 7 2013.

[12] T. O. Wehling, E. ŞaşIoğlu, C. Friedrich, A. I. Lichtenstein, M. I. Katsnelson, and S. Blügel, "Strength of effective coulomb interactions in graphene and graphite," *Physical Review Letters*, vol. 106, 6 2011.

[13] P. R. Wallace, "The band theory of graphite," *Physical Review*, vol. 71, pp. 622–634, 1947.

[14] "Laboratory class scientific computing course book," 2015.

[15] G. Marsaglia, "Xorshift rngs," *Journal of Statistical Software*, vol. 08, 01 2003.

[16] M. Brancher, W. Knauder, M. Piringer, and G. Schauberger, "Temporal variability in odour emissions: To what extent this matters for the assessment of annoyance using dispersion modelling," *Atmospheric Environment: X*, vol. 5, 1 2020.

[17] G. E. Forsythe, "Von neumann's comparison method for random sampling from the normal and other distributions," *Mathematics of Computation*, vol. 26, no. 120, pp. 817–826, 1972. [Online]. Available: http://www.jstor.org/stable/2005864

[18] W. K. Hastings, "Monte Carlo sampling methods using Markov chains and their applications," *Biometrika*, vol. 57, no. 1, pp. 97–109, 04 1970. [Online]. Available: https://doi.org/10.1093/biomet/57.1.97

[19] N. Metropolis, A. W. Rosenbluth, M. N. Rosenbluth, and A. H. T. Teller, "Equation of state calculations by fast computing machines," vol. 1087, 1953.

[20] S. H. T.C., G. K. B., and D. D. B.M., "Ultracold quantum fields," 2009. [Online]. Available: www.springer.com/series/720

[21] Z.-X. Li and H. Yao, "Sign-problem-free fermionic quantum monte carlo: Developments and applications," 5 2018. [Online]. Available: http://arxiv.org/abs/1805.08219http://dx.doi.org/10.1146/annurev-conmatphys-033117-054307

[22] G. Pan and Z. Y. Meng, "Sign problem in quantum monte carlo simulation," 4 2022. [Online]. Available: http://arxiv.org/abs/2204.08777

[23] M. Troyer and U. J. Wiese, "Computational complexity and fundamental limitations to fermionic quantum monte carlo simulations," *Physical Review Letters*, vol. 94, 5 2005.

[24] R. C. Brower, C. Rebbi, and D. Schaich, "Hybrid monte carlo simulation of graphene on the hexagonal lattice," 1 2011. [Online]. Available: http://arxiv.org/abs/1101.5131

[25] M. Ulybyshev, S. Zafeiropoulos, C. Winterowd, and F. Assaad, "Bridging the gap between numerics and experiment in free standing graphene," 4 2021. [Online]. Available: http://arxiv.org/abs/2104.09655

[26] S. Beyl, F. Goth, and F. F. Assaad, "Revisiting the hybrid quantum monte carlo method for hubbard and electron-phonon models," 8 2017. [Online]. Available: http://arxiv.org/abs/1708.03661http://dx.doi.org/10.1103/PhysRevB.97.085144

[27] J. Ostmeyer, E. Berkowitz, S. Krieg, T. A. Lähde, T. Luu, and C. Urbach, "The antiferromagnetic character of the quantum phase transition in the hubbard model on the honeycomb lattice," 5 2021. [Online]. Available: http://arxiv.org/abs/2105.06936http://dx.doi.org/10.1103/PhysRevB.104.155142

[28] T. Luu and T. A. Lähde, "Quantum monte carlo calculations for carbon nanotubes," 11 2015. [Online]. Available: http://arxiv.org/abs/1511.04918http://dx.doi.org/10.1103/PhysRevB.93.155106

[29] M. Körner, D. Smith, P. Buividovich, M. Ulybyshev, and L. V. Smekal, "Hybrid monte carlo study of monolayer graphene with partially screened coulomb interactions at finite spin density," *Physical Review B*, vol. 96, 11 2017.

[30] D. Smith and L. von Smekal, "Hybrid monte-carlo simulation of interacting tight-binding model of graphene," 11 2013. [Online]. Available: http://arxiv.org/abs/1311.1130

[31] J. R. Shewchuk, "An introduction to the conjugate gradient method without the agonizing pain," 1994.

[32] J. C. Sexton and D. H. Weingarten, "P h vs i c s b north-holland hamiltonian evolution for the hybrid monte carlo algorithm," pp. 665–677, 1992.

[33] G. W. Semenoff, "Chiral symmetry breaking in graphene," 8 2011. [Online]. Available: http://arxiv.org/abs/1108.2945http://dx.doi.org/10.1088/0031-8949/2012/T146/014016

[34] J. Bezanson, A. Edelman, S. Karpinski, and V. B. Shah, "Julia: A fresh approach to numerical computing," *SIAM review*, vol. 59, no. 1, pp. 65–98, 2017. [Online]. Available: https://doi.org/10.1137/141000671

[35] R. Breebaart, "Graphenehmc," https://github.com/Rik-Breebaart/GrapheneHMC.git, 2023.

[36] "Iterativesolvers.jl," https://github.com/JuliaLinearAlgebra/IterativeSolvers.jl.git, 2022.

[37] J. Ostmeyer, E. Berkowitz, S. Krieg, T. A. Lähde, T. Luu, and C. Urbach, "The semimetal-mott insulator quantum phase transition of the hubbard model on the honeycomb lattice," 5 2020. [Online]. Available: http://arxiv.org/abs/2005.11112http://dx.doi.org/10.1103/PhysRevB.102.245105

[38] M. D. Hoffman and A. Gelman, "The no-u-turn sampler: Adaptively setting path lengths in hamiltonian monte carlo," pp. 1593–1623, 2014. [Online]. Available: http://mcmc-jags.sourceforge.net

# Appendix A

# Integration Saxton Weingarten

In this appendix section, a short description of the Sexton-Weingarten (SW)[32] integrator is given. This integrator improves upon leap frog integration by using a different step-size dependent on the component of the derivatives. This method is used to improve the integration accuracy, which will allow for larger time steps in the integration and lead to an increase in computation speed.

Let us consider a Hamiltonian of the form

$$\mathcal{H} = \frac{\pi^T \pi}{2} + S_1(\phi) + S_2(\phi), \tag{A.1}$$

for which the number of operations to evaluate $S_1$ is much smaller than those to evaluate $S_2$.
With this Hamiltonian the force $F = d\pi/dt$, where $\pi$ is the momentum, would be composed of different components $F_i$ which differ both in magnitude and associated computation cost. The SW integrator uses this difference to improve the efficiency of the integrator (compared to leap frog). This is done by performing an integration step on the momentum field with a force with multiple step sizes for the different components. In the case we have a force of the form

$$F = F_1 + F_2, \tag{A.2}$$

the integration step of the momentum can be split into one step of $\epsilon$, using the derivative $F_1$, and then perform $m_{sw}$ steps of $\epsilon/m_{sw}$ of derivative $F_2$. For leapfrog integration, the momentum step $V_\pi(\epsilon)$ and position step $V_\phi(\epsilon)$ are

$$\begin{aligned} V_\pi(\epsilon) : \pi_{\tau+1} &= \pi_t - \epsilon(\frac{\partial \mathcal{H}}{\partial \phi}), \\ V_\phi(\epsilon) : \phi_{\tau+1} &= \phi_t + \epsilon(\frac{\partial \mathcal{H}}{\partial \pi}). \end{aligned} \tag{A.3}$$

Leapfrog integration consists of iterating these steps as either

$$V_\pi(\epsilon/2)V_\phi(\epsilon)V_\pi(\epsilon/2) \quad \text{or} \quad V_\phi(\epsilon/2)V_\pi(\epsilon)V_\phi(\epsilon/2) \tag{A.4}$$

For SW integration, the momentum step $V_p(\epsilon)$ with step size $\epsilon$ is split into multiple steps as

$$V_\pi(\epsilon) \to V_\pi^{F_1}(\frac{\epsilon}{2})\big[V_\pi^{F_2}(\frac{\epsilon}{m_{sw}})\big]^{m_{sw}} V_\pi^{F_1}(\frac{\epsilon}{2}), \tag{A.5}$$

where $V_\pi^{F_i}(\epsilon)$ is the momentum step using only one of the force components.

# Appendix B

# Hubbard-Stratonovich transformation

In rewriting the action in terms of fermionic matrices and an interaction component, the quartic interaction terms are removed by means of a Hubbard-Stratonovich (HS) transformation. This transformation adds an additional field to the theory, the HS field $\phi$. To perform the HS transformation used for the BRS method[24], for which we needed to obtain the desired complex contribution of the HS field, specific care has to be taken in the transformation.

The quartic interaction component of the theory is given by

$$e^{-\sum_{i,j} Q_i A_{ij} Q_j}, \tag{B.1}$$

for which the indices $i, j$ run over the time and space dimensions $x, t$. Here we have taken a general matrix $A_{ij}$ however in the case of our theory this will be the Coulomb interaction matrix such that $A_{(x,t)(y,t')} = V_{x,y}\delta_{t,t'}$.

To perform the HS transformation, we will look at the following Gaussian integral

$$\int \mathcal{D}\phi e^{-\sum_{i,j} \phi_i A_{ij}^{-1} \phi_j}, \tag{B.2}$$

which satisfies

$$\int \mathcal{D}\phi e^{-\sum_{i,j} \phi_i A_{ij}^{-1} \phi_j} = \int \mathcal{D}\tilde{\phi} e^{-\sum_{i,j} \tilde{\phi}_i A_{ij}^{-1} \tilde{\phi}_j}, \tag{B.3}$$

where $\tilde{\phi} = \phi + iqA$. To allow for our integral to be rewritten in such form, we need to know if the given shift along the imaginary plane is possible. For this, we will look at the Contour integral that describes this shift (see fig.B.1). The contour integral is given by

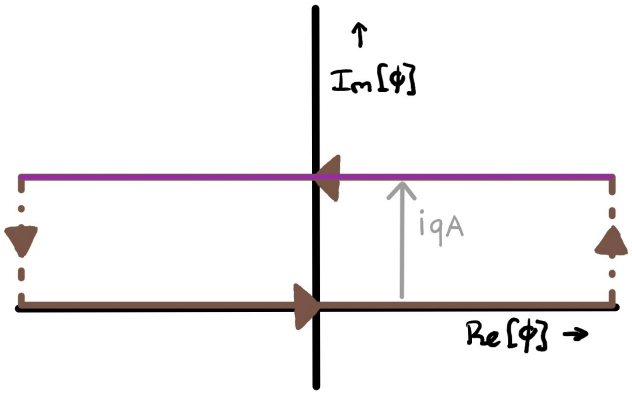


Figure B.1: Contour integral of the shift of a Gaussian integral into the complex plane.

$$\begin{aligned}\int_{\mathcal{C}} \mathcal{D}\phi e^{-\phi^T A^{-1}\phi} =& \int_{-\infty}^{\infty} \mathcal{D}\phi e^{-\phi^T A^{-1}\phi} + \int_{0}^{iqA} \mathcal{D}\alpha e^{-(u+\alpha)^T A^{-1}(u+\alpha)}|_{u=\infty} \\ &+ \int_{\infty}^{-\infty} \mathcal{D}\tilde{\phi} e^{-\tilde{\phi}^T A^{-1}\tilde{\phi}} + \int_{iqA}^{0} \mathcal{D}\alpha e^{-(u+\alpha)^T A^{-1}(u+\alpha)}|_{u=-\infty} \\ =& 2\pi i \sum_{j=1}^{N} \mathrm{Res}[e^{-\phi^T A^{-1}\phi}],\end{aligned} \tag{B.4}$$

where we used vector/matrix notation. If integrand has no singular points then

$$\mathrm{Res}[e^{-\phi^T A^{-1}\phi}] = 0. \tag{B.5}$$

The side contours at the positive and negative infinite real axis point both are zero given that $\mathrm{Re}[A^{-1}] > 0$, since then the limit takes the exponential term to zero. We thus have that

$$\int_{-\infty}^{\infty} \mathcal{D}\phi e^{-\phi^T A^{-1}\phi} = \int_{-\infty}^{\infty} \mathcal{D}\phi e^{-(\phi+iqA)^T A^{-1}(\phi+iqA)} \tag{B.6}$$

with $\tilde{\phi} = \phi + iqA$, requiring that $\mathrm{Re}[A^{-1}] \geq 0$ and that $e^{-\phi A^{-1}\phi}$ has no singularities within the contour region. In the case of our Coulomb interaction, both these properties are satisfied. The coulomb potential $V_{x,y}$ obeys that $\mathrm{Re}[V_{x,y}^{-1}] \geq 0$ for all $x, y$ and there are therefore also no singularities within the contour.

Now that we know that we can perform the shift within our integral, we can use this to rewrite the interaction term Eq.(B.1) as

$$e^{-\sum_{i,j} Q_i A_{ij} Q_j} = C e^{-\sum_{i,j} Q_i A_{ij} Q_j} \int \mathcal{D}\phi e^{\sum_{i,j} \phi_i A_{ij}^{-1} \phi_j} \tag{B.7}$$

where $C = \frac{\sqrt{\mathrm{Det}(A^{-1})}}{2(2\pi)^{N/2}}$ using that the Gaussian integral

$$\int \mathcal{D}\phi e^{-\phi^T A^{-1}\phi} = \frac{2(2\pi)^{N/2}}{\sqrt{\mathrm{Det}(A^{-1})}}, \tag{B.8}$$

where $N$ is the dimension of the $\phi$ field. If we now perform our shift along the imaginary axis this result in

$$\begin{aligned} e^{-\sum_{i,j} Q_i A_{ij} Q_j} &= C e^{-\sum_{i,j} Q_i A_{ij} Q_j} \int \mathcal{D}\tilde{\phi} e^{-\sum_{i,j} (\phi + iQ^T A)_i A_{ij}^{-1} (\phi + iQ^T A)_j} \\ &= C \int \mathcal{D}\tilde{\phi} e^{-\sum_{i,j} \phi_i A_{ij}^{-1} \phi_j - 2i \sum_i Q_i \phi_i}. \end{aligned} \tag{B.9}$$

# Appendix C

# Sublattice spin difference results at different masses

In this appendix section, the sublattice spin difference measurements discussed in section 6.1 are shown for the different masses.

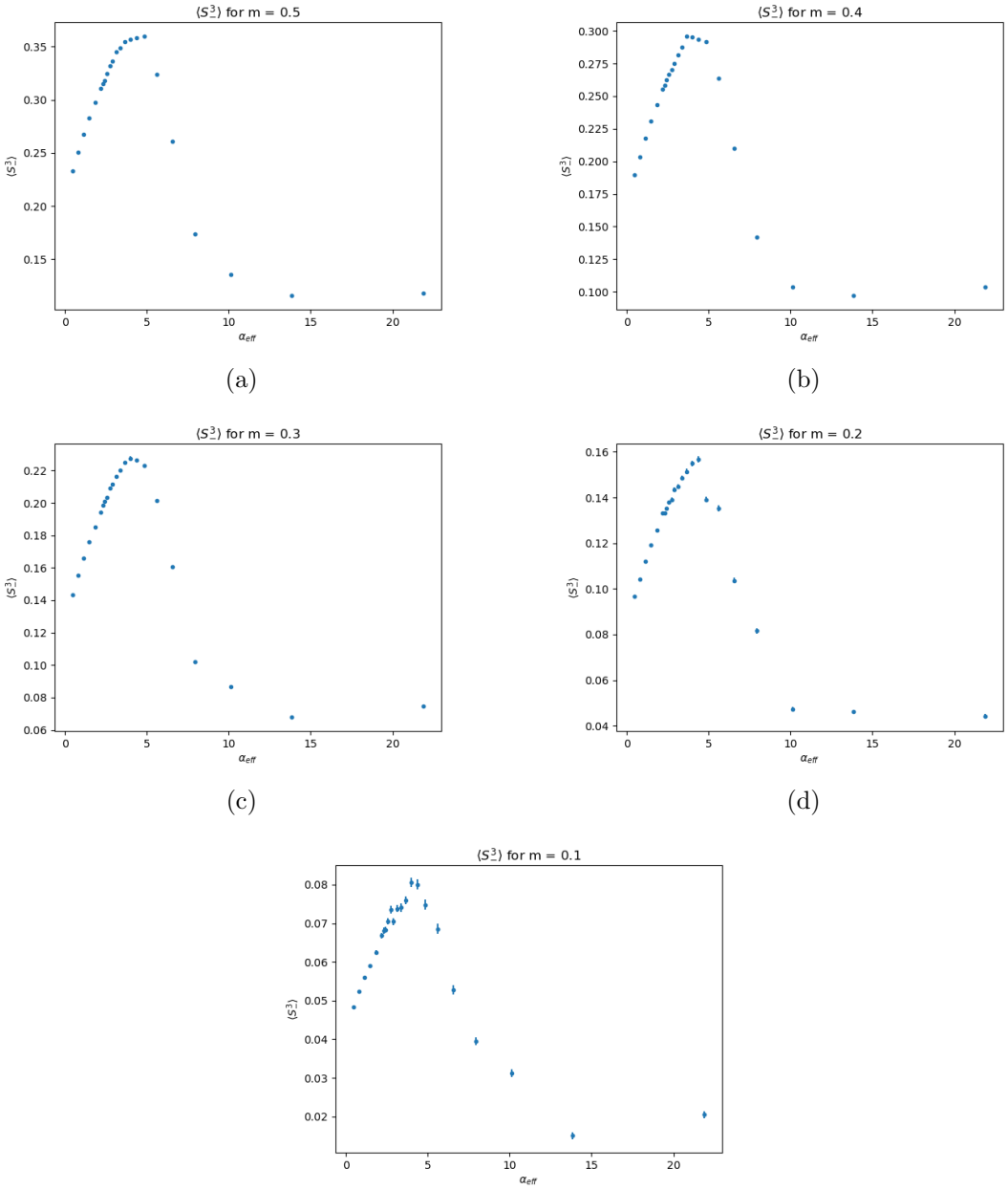


(a) (b) (c) (d) (e)

Figure C.1: Calculation results for the sublattice spin difference $\langle S^3_- \rangle$ for a system of $L_m = 4$, $L_n = 4$ with $N_t = 16$ for the different masses.